Into the blue...Using mouse models to uncover genes driving tumorigenesis and therapy resistance in human breast cancer

Ruiter, J.R. de

7

Selective loss of PARG restores PARylation and counteracts PARP inhibitor-mediated synthetic lethality

Ewa Gogola[1,14], Alexandra A. Duarte[1,14,*], Julian R. de Ruiter[1,2,14,*], Wouter W. Wiegant[6], Jonas A. Schmid[7], Roebi de Bruijn[1,2,14], Dominic I. James[8], Sergi Guerrero Llobet[9], Daniel J. Vis[2,14], Stefano Annunziato[1,14], Bram van den Broek[3], Marco Barazas[1,14], Ariena Kersbergen[5], Marieke van de Ven[4], Madalena Tarsounas[10], Donald J. Ogilvie[8], Marcel van Vugt[9], Lodewyk F.A. Wessels[2,14], Jirina Bartkova[11,12], Irina Gromova[11], Miguel Andújar-Sánchez[13], Jiri Bartek[11,12], Massimo Lopes[7], Haico van Attikum[6], Piet Borst[5], Jos Jonkers[1,14,17], Sven Rottenberg[1,15,16,17]

[1] Division of Molecular Pathology, The Netherlands Cancer Institute, Amsterdam, the Netherlands
[2] Division of Molecular Carcinogenesis, The Netherlands Cancer Institute, Amsterdam, the Netherlands
[3] Division of Cell Biology and BioImaging Facility, The Netherlands Cancer Institute, Amsterdam, the Netherlands
[4] Mouse Clinic for Cancer and Aging (MCCA), Preclinical Intervention Unit, The Netherlands Cancer Institute, Amsterdam, the Netherlands
[5] Division of Molecular Oncology, The Netherlands Cancer Institute, Amsterdam, the Netherlands
[6] Department of Human Genetics, Leiden University Medical Center, Leiden, the Netherlands
[7] Institute of Molecular Cancer Research, University of Zurich, Zurich, Switzerland
[8] Drug Discovery Unit, Cancer Research UK, University of Manchester, Manchester, UK
[9] Department of Medical Oncology, University Medical Center Groningen, University of Groningen, Groningen, the Netherlands
[10] CRUK/MRC Oxford Institute for Radiation Oncology, University of Oxford, Oxford, UK
[11] Danish Cancer Society Research Center, Copenhagen, Denmark
[12] Karolinska Institute, Department of Medical Biochemistry and Biophysics, Division of Genome Biology, Science for Life Laboratory, Stockholm, Sweden
[13] Pathology Department, Complejo Hospt. Univ. Insular Materno Infantil, Las Palmas, Spain
[14] Cancer Genomics Netherlands, Oncode Institute, Amsterdam, the Netherlands
[15] Institute of Animal Pathology, Vetsuisse Faculty, University of Bern, Bern, Switzerland
[16] Lead contact
[17] Correspondence: j.jonkers@nki.nl (J.J.), sven.rottenberg@vetsuisse.unibe.ch (S.R.)
[*] These authors contributed equally to this work

Published in Cancer Cell, 11 June 2018
Volume 33, Issue 6, Pages 1078-1093

7.1 Summary

Inhibitors of poly(ADP-ribose) (PAR) polymerase (PARPi) have recently entered the clinic for the treatment of homologous recombination (HR)-deficient cancers. Despite the success of this approach, drug resistance is a clinical hurdle, and we poorly understand how cancer cells escape the deadly effects of PARPi without restoring the HR pathway. By combining genetic screens with multi-omics analysis of matched PARPi-sensitive and -resistant *Brca2*-mutated mouse mammary tumors, we identified loss of PAR glycohydrolase (PARG) as a major resistance mechanism. We also found the presence of PARG-negative clones in a subset of human serous ovarian and triple-negative breast cancers. PARG depletion restores PAR formation and partially rescues PARP1 signaling. Importantly, PARG inactivation exposes vulnerabilities that can be exploited therapeutically.

7.2 Significance

To explore defects in the DNA damage response in cancer therapy, exciting opportunities have been achieved using the 'synthetic lethal' approach. A successful example is the development of PARP inhibitors to kill cancer cells that are defective in HR; e.g., due to lack of function of BRCA1 or BRCA2. Thus, there is a real opportunity to cure patients with HR-deficient cancers if we overcome the hurdle of drug resistance. At present, it is largely unknown how tumor cells escape PARP inhibition without restoring BRCA2-mediated HR. Here, we show that loss of PARG governs PARPi resistance in HR-deficient tumors by restoring PARP1 signaling. Importantly, inactivation of PARG results in vulnerabilities that can be exploited to combat resistance.

7.3 Introduction

Defects in the DNA damage response (DDR) result in genomic instability and are implicated in many types of cancer[1]. DDR alterations are responsible for the accumulation of mutations that result in tumorigenesis, and they can be specifically exploited for targeted cancer therapy. A prime example of such a tailored approach is the application of poly (ADP-ribose) polymerase (PARP) inhibitors (PARPi) in the treatment of tumors defective in homology-directed DNA repair due to BRCA1 or BRCA2 inactivation[2,3]. PARP1, a founding member of the PARP family, is a nuclear protein functioning in various cellular processes, including chromatin remodeling and DNA damage repair[4]. Upon DNA damage, PARP1 is rapidly recruited to DNA nicks where it induces the synthesis of protein-conjugated polymers of ADP-ribose

(poly(ADP-ribose) [PAR]). PARP1 itself is a prime target of PARylation and the resulting PAR chains serve as a platform for the recruitment of downstream repair factors. PARylation is a transient and reversible modification, as it is counteracted by the activity of PAR glycohydrolase (PARG), which degrades PAR[5]. Inhibition of PARP1 leads to the accumulation of unresolved single-strand breaks (SSBs)[6]. Moreover, several PARPi trap PARP1 onto chromatin[7,8], resulting in the collapse of replication forks (RF) that hit trapped PARP1. This leads to DNA double-strand breaks (DSBs) and cells depend on BRCA1/2-mediated repair to resolve these DSBs in an error-free way. Hence, PARP1 inhibition causes synthetic lethality in tumors with defects in homologous recombination (HR)[2,3]. Indeed, this lethality was also observed in mouse models for *BRCA1/2*-mutated breast cancer[9,10] as well as in patients with *BRCA1/2* mutations who developed breast or ovarian cancer[11–13]. On the basis of these positive clinical results, three different PARPi were recently approved as a monotherapy for the treatment of *BRCA1/2*-mutated ovarian cancers[14].

Drug resistance often follows the introduction of therapeutics in the clinic, and unfortunately PARPi are no exception[11,12]. Using cell lines and mouse models, several mechanisms of PARPi resistance have been identified, including upregulation of the P-glycoprotein (P-gp; also known as ABCB1) drug efflux transporter[9,10] and restoration of HR activity (reviewed by Annunziato *et al.*[15]). While the clinical significance of P-gp-driven resistance remains controversial, HR restoration has been observed in human tumors that re-established BRCA1/2 function[16,17]. Nevertheless, secondary *BRCA1/2* mutations explain only some of the cases of PARPi resistance[18]. The requirement of BRCA1 for HR activity can be bypassed by the loss of the 53BP1-RIF1-REV7 pathway, as shown by various studies[15]. In contrast, there is no evidence that HR can be rescued in the absence of BRCA2, suggesting that BRCA2-deficient tumors employ distinct, HR-independent pathways to overcome PARPi toxicity.

Little is known thus far about HR-independent resistance to PARPi. Loss of the drug target PARP1 has been described as a mechanism of resistance in HR-proficient cells[19], but this cannot explain resistance in the PARPi target group, since PARP1 loss causes synthetic lethality of *BRCA1/2*-mutated cells[2,3]. In this study, we set out to determine how cells with an irreversible and complete defect in the HR pathway develop PARPi resistance.

7.4 Results

7.4.1 Functional genetic screens identify loss of PARG as a PARPi resistance factor

To identify HR-independent mechanisms of PARPi resistance, we carried out functional genetic screens in two types of *in vitro* cultures that we derived from *Brca2*$^{-/-}$*;p53*$^{-/-}$ mouse mammary tumors from *K14cre;p53*$^{F/F}$*;Brca2*$^{F/F}$ (KB2P) mice: two-dimensional (2D) tumor cell lines (KB2P1.21, KB2P3.4) and three-dimensional (3D) cancer organoids (ORG-KB2P26S.1)[9,20,21]. In these cells we introduced a library of 1,976 short hairpin RNA (shRNA) constructs targeting 391 DDR-related genes (on average five shRNAs/gene)[22]. The cells were then selected for 3 weeks with the PARPi olaparib or AZD2461 (Figure 7.1A) at a concentration lethal to the parental cells (data not shown). Sequencing of PARPi-surviving populations revealed a reproducible enrichment of multiple hairpins targeting PARG. The strong effect of PARG depletion is reflected by the overall top score of *Parg* among all positively selected genes, as determined by the MAGeCK (Model-based Analysis of Genome-wide CRISPR-Cas9 Knockout) algorithm[23] (Figure 7.1B-C; Table S7.1). We applied the same screening approach to a cell line isolated from BRCA-proficient mouse mammary tumors from *K14cre;p53*$^{F/F}$ (KP) mice[9] and also identified *Parg* among the top outliers. In fact, *Parg* was the only common hit in both BRCA-deficient and -proficient screens (Figure 7.1D-E). In contrast, shRNAs targeting PARP1 were only enriched in the BRCA-proficient KP3.33 cells (Figure 7.1C-E), providing functional evidence that PARP1 loss confers PARPi resistance in BRCA-proficient cells, presumably by preventing PARP1 trapping, but not in BRCA2-deficient cells that depend on PARP1 for survival.

7.4.2 PARG is frequently lost in PARPi-Resistant KB2P mouse mammary tumors

Although high-throughput genetic screens are powerful tools for the identification of gene candidates, *in vitro* conditions do not fully recapitulate the complexity of drug response observed in real tumors. We therefore generated a panel of KB2P mouse mammary tumors that had acquired PARPi resistance *in vivo*. For this purpose, 21 individual spontaneous KB2P carcinomas were orthotopically transplanted into multiple syngeneic mice to allow differential treatment of the original donor tumor. Upon outgrowth, the tumors were either treated with vehicle control or with the PARPi AZD2461 (Figure 7.2A). As expected, KB2P tumors were initially highly sensitive to PARPi treatment but eventually developed drug resistance (Figure 7.2B-

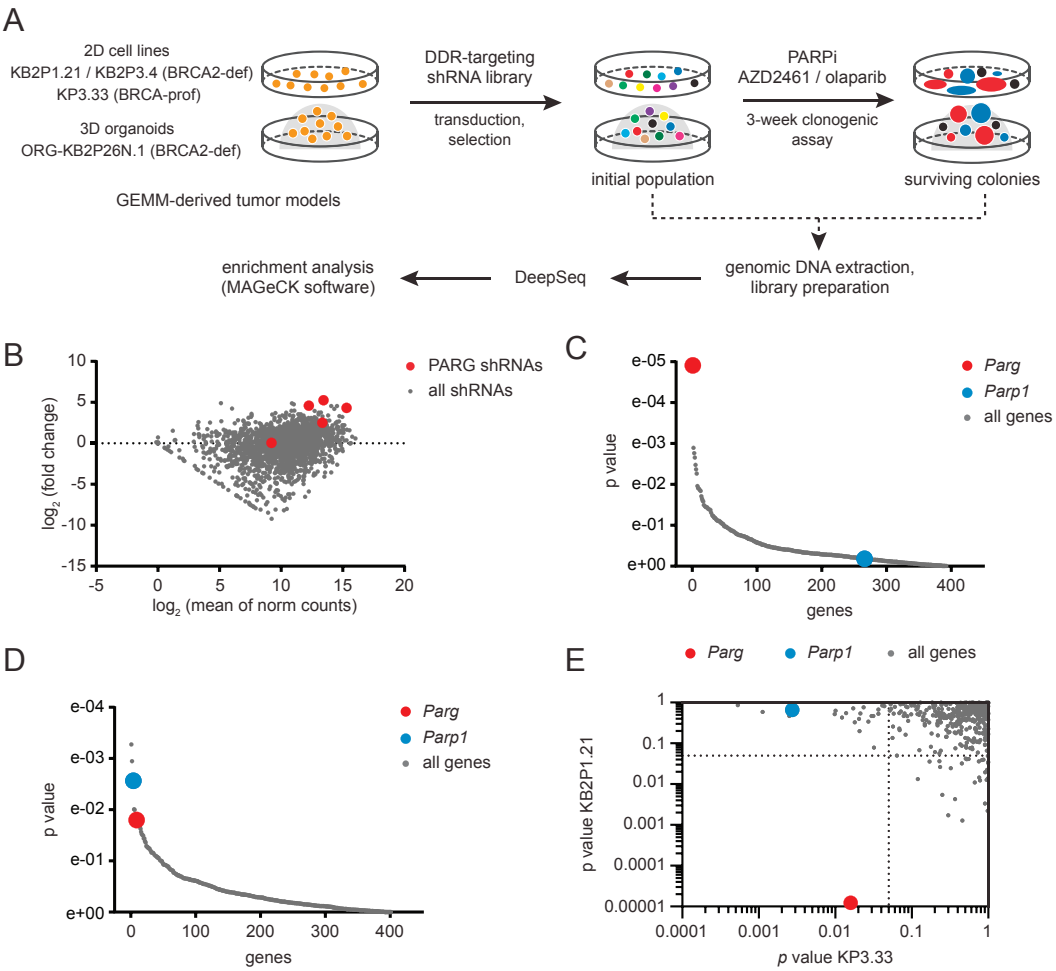

Fig. 7.1. Functional shRNA-based screens in BRCA2-deficient and -proficient cells identify PARG as PARPi resistance factor. (A) Outline of the functional shRNA screen. **(B)** Log ratio (fold change) versus abundance (mean of norm counts) plot representing the screening outcome in KB2P1.21 cells treated with AZD2461. **(C-D)** Distribution of the one-sided p value (gene enrichment) for all 391 genes targeted by the shRNA-based library in KB2P1.21 cells (C) and KP3.33 (D) cells upon PARPi treatment. **(E)** Comparison of the screening outcome between indicated cell lines; dotted grid line indicates p value = 0.05. All p values were generated per gene with MAGeCK software; each screen was performed and analyzed in triplicate. See also Table S7.1.

C). The observed resistance cannot be explained by BRCA2 restoration, which is prevented by the irreversible intragenic deletion in *Brca2*, nor by upregulation of P-gp (Figure S7.1A), because of the low affinity of AZD4261 to this transporter[24,25].

Our extensive *in vivo* studies yielded a unique collection of matched PARPi-naive ($n = 21$) and PARPi-resistant tumors ($n = 34$; for some of the donors more than one resistant tumor was generated). We have recently shown that the resistance phenotype is stable upon transplantation into allografts[21,26]. We now used this collection of tumors to identify genetic factors contributing to PARPi resistance. For this purpose, we generated transcriptome (RNA sequencing [RNA-seq]) and

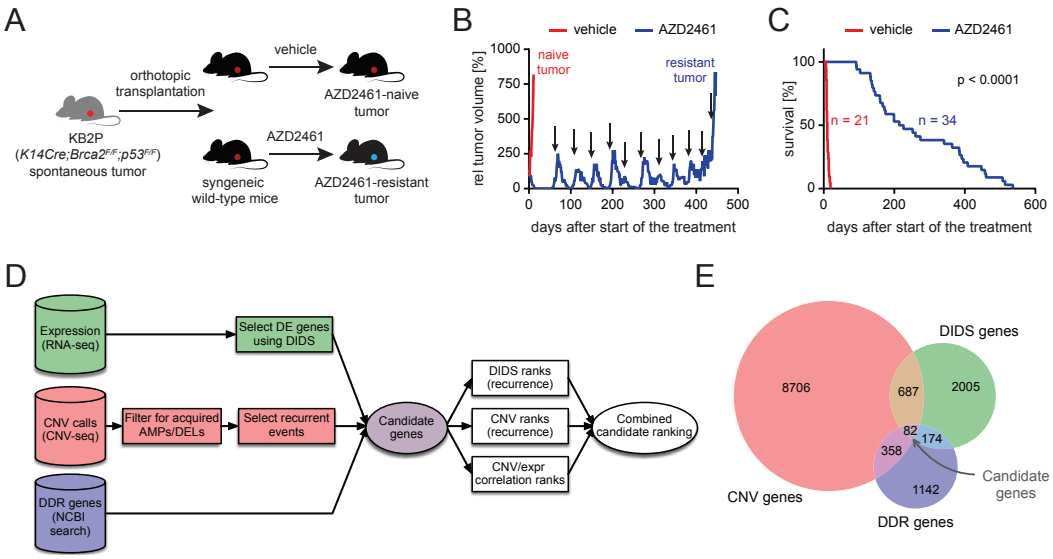

Fig. 7.2. PARG is frequently lost in KB2P Tumors that acquired PARPi resistance *in vivo*. **(A)** Generation of matched PARPi-naive and -resistant KB2P tumors. **(B)** Treatment response of individual KB2P tumor treated with either vehicle or AZD2461, orally for 28 consecutive days. Treatment was resumed when the tumors reached a size of 100% (initial volume at the start of the treatment) and the treatment cycles were repeated until acquired resistance (black arrows mark the beginning of repeated cycles). Graph shows relative tumor volume as a function of time. **(C)** Kaplan-Meier curve showing overall survival of mice bearing KB2P tumors treated with either vehicle or AZD2461. Log rank (Mantel-Cox) p value is indicated. **(D)** Flowchart illustrating the steps of multi-omics approach used for the discovery of resistance factors in a panel of KB2P tumors. **(E)** Venn diagram showing overlap of potential gene candidates identified within indicated datasets.

DNA copy number variation (CNV) sequencing (CNV-seq) data for all tumors and carried out an integrative analysis of naive versus resistant samples (Figure 7.2D-E). First, we identified differentially expressed genes using the DIDS (detection of imbalanced differential signal) algorithm (cutoff $p < 0.05$), which is specifically designed for the detection of subgroup markers in heterogeneous populations[27]. In parallel, we selected acquired copy number events, present only in resistant, but not in naive, samples. Since KB2P tumors exhibit high levels of genomic instability and accumulate many genetic alterations, we decided to focus on DDR-related genes, as their contribution to the PARPi response is most plausible. We generated a list of approximately 1,800 genes that have been implicated in DDR processes (Table S7.2) and combined it with the significant hits from the DIDS and CNV analyses. The 82 genes that survived these selection criteria were ranked based on their recurrence or correlation between expression and CNV data. To integrate these rankings, we used three different aggregation statistics: mean aggregation, Stuart aggregation, and robust rank aggregation (RRA)[28]. Consistent with our *in vitro* screens, all three algorithms placed *Parg* at the top of the list of gene candidates (Table S7.3). *Parg* also ranked among the top outliers in a non-curated,

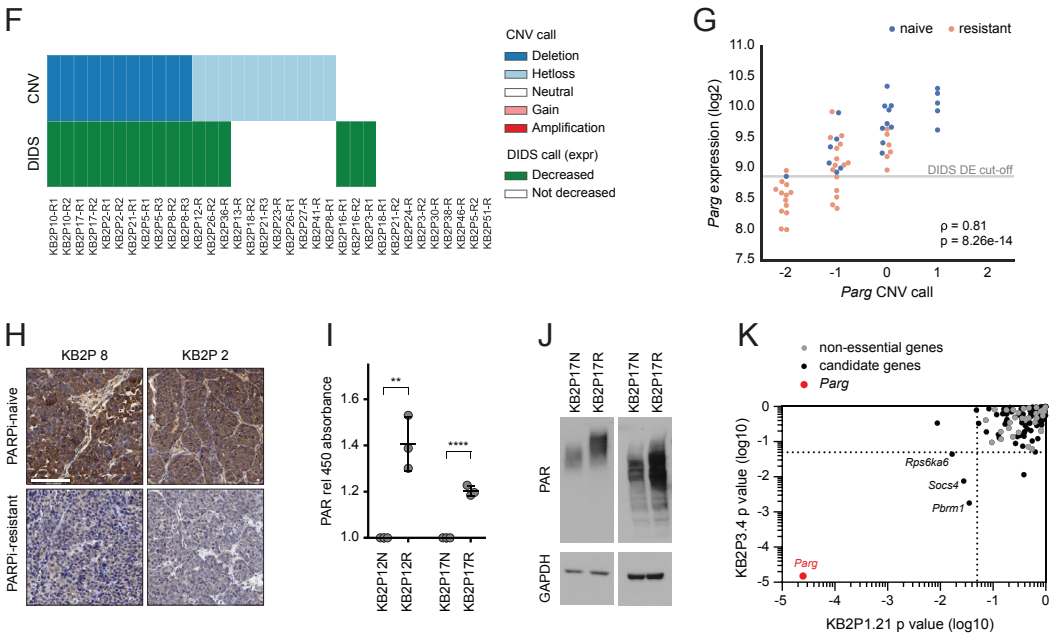

Fig. 7.2. **Continued.** **(F)** Overview of genomic alterations in *Parg* acquired by a panel of 34 KB2P PARPi-resistant tumors (KB2Px-Ry: x, original donor identification [ID] number; y, ID of individual resistant tumors derived from the same donor tumor). **(G)** Correlation between *Parg* expression and copy number estimation for the whole panel of KB2P tumors. Spearman correlation coefficient (ρ), p value, and expression threshold generated by DIDS algorithm (gray line) are indicated. **(H)** Representative images of PARG IHC staining in KB2P tumors; scale bar, 100 μm. **(I)** ELISA-based PARG activity assay in tumor organoids (N, naive; R, resistant); $^{**}p < 0.01$, $^{****}p < 0.0001$ (two-tailed t-test); experiment repeated three times, data presented as mean $\pm$ SD of replicates. **(J)** Western blot analysis of PAR in tumor-derived organoids; data representative of two independent experiments. **(K)** Enrichment analysis of the secondary genetic screen in KB2P cells: comparison of the p values for all genes targeted, shown for the cell lines indicated; one-sided p value was determined by the MAGeCK algorithm; the screen was performed in triplicate. See also Figure S7.1 and Tables S7.1 to S7.4.

genome-wide comparison (Table S7.3). In our panel of 34 PARPi-resistant tumors, we observed decreased expression of *Parg* in 17 tumors, and acquired copy number loss of the *Parg* locus in 22 tumors (11 deletions, 11 heterozygous loss events), with a substantial overlap between both datasets (Figure 7.2F-G and S1B). The difference in PARG levels between PARPi-naive and -resistant tumors was also confirmed by immunohistochemistry (IHC) (Figure 7.2H). Blinded semi-quantitative analysis of the PARG staining revealed a significant difference between resistant versus naive samples ($p < 0.015$, Mann-Whitney U test). This was further validated using an ELISA assay in which we monitored the loss of biotinylated PAR from immobilized histones and thereby directly measured the relative activity of endogenous PARG in 3D cancer organoids derived from PARG-deficient PARPi-resistant tumors and PARPi-sensitive controls (Figure 7.2I). As expected, PARPi-resistant organoids showed reduced ability to degrade synthetic PAR (Figure 7.2I) and overall exhibited elevated levels of endogenous PAR (Figure 7.2J).

To investigate the contribution of the other candidate genes to PARPi resistance, we performed a secondary genetic loss-of-function screen using an shRNA library targeting the identified candidates and 32 non-essential genes as internal controls (Table S7.4). *Parg* was again identified as a top outlier by the enrichment analysis in both KB2P cell lines (Figure 7.2K and Table S7.1), suggesting that loss of PARG is one of the strongest mechanisms involved in PARPi resistance in our model.

To test whether PARPi-induced loss of PARG is specific to KB2P tumors, we also studied genetic alterations in *Parg* in our previously described collection of PARPi-naive and -resistant BRCA1-deficient mammary tumors from *K14cre;Brca1F/F;Trp53F/F* (KB1P) mice[24]. Also in this cohort, combined RNA-seq and CNV-seq analysis identified several PARPi-resistant tumors with significantly lower expression and acquired copy number loss of *Parg* (Figure S7.1C). Taken together, our *in vivo* data confirm and extend the results from the *in vitro* screens and suggest that PARG depletion alleviates PARPi toxicity.

7.4.3 PARG downregulation causes PARPi resistance *in vitro*

To validate the role of PARG depletion in PARPi resistance, we introduced two individual shRNAs against PARG (PARG sh1, PARG sh4) in KB2P1.21 and KB2P3.4 cells, resulting in substantial decrease of *Parg* mRNA levels (Figure 7.3A and Figure S7.2A) and reduced PARG activity (Figure 7.3B and Figure S7.2B) Consistently, genetic depletion of PARG in KB2P cells led to the accumulation of PAR under genotoxic stress induced by the alkylating agent methyl methanesulfonate (MMS) (Figure S7.2C-D) but did not affect *Parp1* expression levels (Figure S7.2E).

The shRNA-mediated loss of PARG resulted in increased resistance to the PARPi olaparib and AZD2461 in long-term clonogenic survival assays. This effect was observed in cell lines derived from both KB2P and KB1P tumor models, in which PARPi-induced loss of PARG was observed *in vivo* (Figure 7.3C and Figure S7.3A-C). To exclude off-target effects of the shRNAs, we also targeted the *Parg* locus in KB2P cells using CRISPR-Cas9 technology (Figure 7.3D and Figure S7.3D-F). In contrast to the control cells, *Parg*-targeted cells formed many resistant colonies after 14 days of PARPi selection. This effect was specific to Parg inactivation, as shown by the TIDE (Tracking of Indels by Decomposition) analysis[29]. In the initial tumor cell population, roughly half of the alleles carried frameshift mutations, and vehicle (DMSO) treatment did not significantly affect allele composition. In contrast, PARPi selection resulted in a substantial increase in frameshift disruptions ($> 90\%$), showing that the surviving populations are predominantly PARG deficient (Figure 7.3D and Figure S7.3D-F, Table S7.5).

We obtained further evidence for the role of PARG in PARPi resistance with a recently developed small-molecule PARG inhibitor (PARGi) PDDX-004 (PDD00017272), which is very active against mouse PARG[30]. In line with this, PDDX-004 caused a dose-dependent accumulation of nuclear PAR upon MMS-induced DNA damage in our cell lines (Figure S7.3G-H). Consistent with our genetic inhibition experiments, the clonogenic assays in KB2P cells also showed an increased PARPi survival upon chemical inhibition of PARG (Figure 7.3E and Figure S7.3I). Moreover, the viability of cells exposed to the combination of PARPi and PARGi correlated with the degree of PARG inhibition, while PDDX-004 alone did not affect cell growth nor PARPi response of PARG-depleted cells (Figure S7.3J). In conclusion, both genetic depletion or inactivation and chemical inhibition of PARG lead to PARPi resistance in KB2P cells, confirming an important functional role of PARG in mediating PARPi toxicity.

7.4.4 PARG-Depleted KB2P cells remain HR deficient and fail to protect stalled RFs

The sequence of events that leads to PARPi-induced death of BRCA-deficient cells includes the inhibition of PAR synthesis, RF collapse, and the formation of DSBs. In collaboration with the Nussenzweig laboratory, we have recently shown that RF protection can explain resistance in some of the PARPi-resistant KB2P mouse mammary tumors[26]. Given its role in PAR catabolism, however, we did not expect that the tumors in which we find PARG downregulation would correct the BRCA2 defect by protecting stalled RFs or by BRCA2-independent restoration of HR. To verify this, we measured the capacity of PARG-depleted KB2P cells to protect stalled RF using DNA fiber assays. In both control and PARG knockdown KB2P cells, the induction of replication stress resulted in the degradation of nascent tracts (Figure S7.4A), suggesting that PARG loss cannot bypass the requirement of BRCA2 for RF stabilization. Next, we assessed the capability of KB2P cells to form RAD51 ionizing radiation (IR)-induced foci (IRIF), a hallmark of HR activity. As expected, we did not detect any RAD51 IRIF in KB2P cells, regardless of *Parg* expression levels (Figure S7.4B-C). Moreover, the same phenotype was observed in PARPi-resistant KB2P tumors, in which PARG loss was confirmed at the genomic level (Figure S7.4D). These results demonstrate that loss of PARG causes PARPi resistance independently of BRCA2 and that resistance cannot be explained by HR restoration or RF protection.

7.4.5 PARG downregulation rescues PARylation upon PARPi treatment

To assess how PARG depletion causes PARPi resistance, we studied its effect on PARylation. Upon PARPi treatment, inhibition of PARP enzymes serves as the major

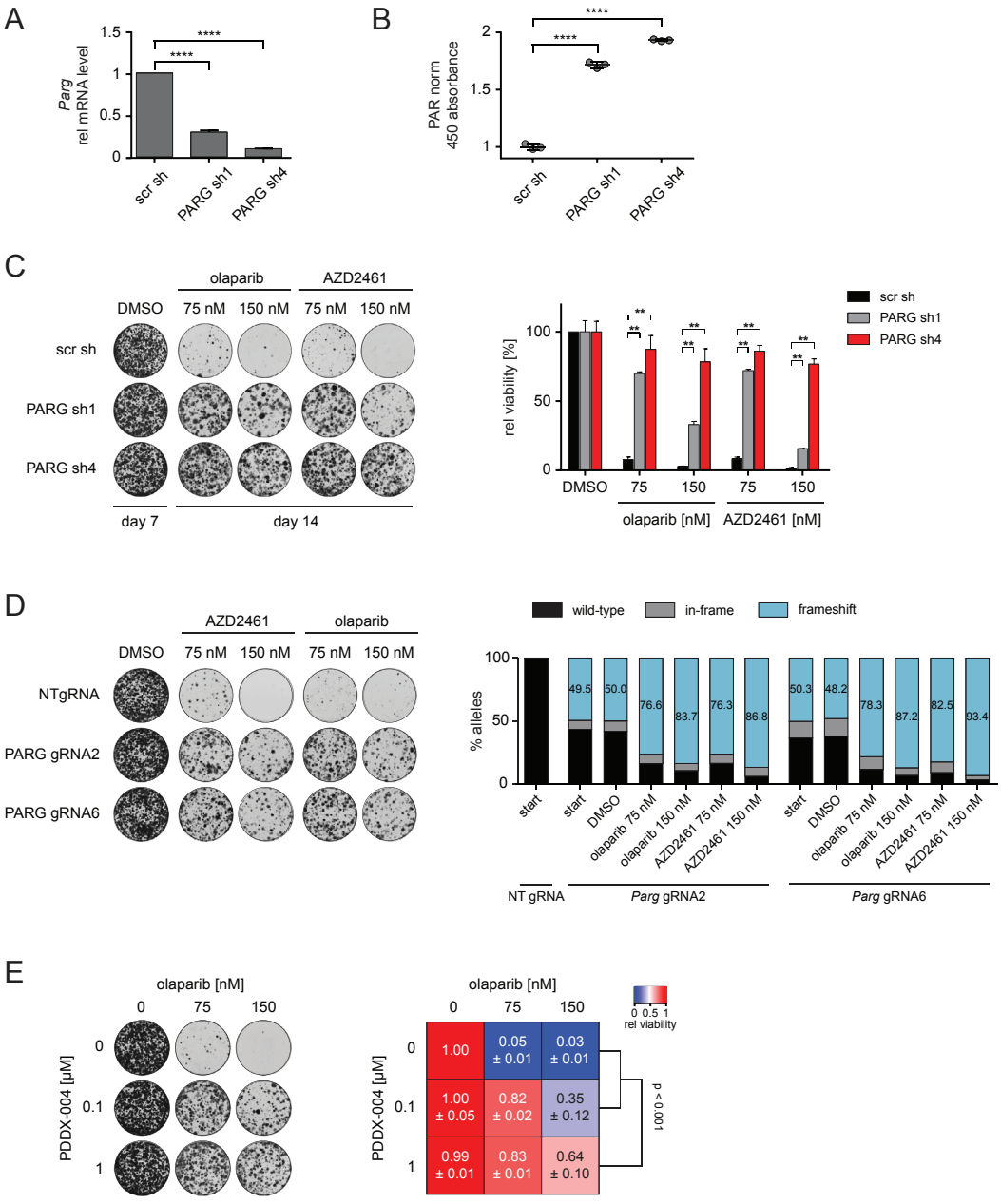

Fig. 7.3. Downregulation of PARG causes PARPi resistance in BRCA2-deficient cells *in vitro*. **(A)** RT-qPCR analysis of *Parg* expression levels in KB2P1.21 cell lines expressing indicated shRNAs; data represent mean ± SD of triplicate; $^{****}p < 0.001$ (two-tailed t-test). **(B)** PAR ELISA assay in KB2P1.21 cells; data shown as mean ± SD of triplicate, $^{****}p < 0.001$ (two-tailed t-test). **(C)** Representative images (left) and quantification (right) of long-term clonogenic assay with KB2P1.21 cells, treated with PARPi or untreated (DMSO). Data represent mean ± SD of three independent repeats; $^{**}p < 0.01$ (t-test). **(D)** Representative images (left) and TIDE quantification (right) of long-term clonogenic assay with KB2P1.21 cells expressing indicated guide RNAs. **(E)** Representative images (left) and quantification (right) of long-term clonogenic assay with KB2P1.21 cells treated as indicated. The experiment was repeated three times; data plotted as mean ± SD; $p < 0.001$ (ANOVA). See also Figures S7.2 and S7.3 and Table S7.5.

barrier to PAR formation, but this is reinforced by the PARG-mediated degradation of PAR, which acts in the same direction as PARPi. We therefore hypothesized that PARPi alone does not fully inhibit PARP and loss of PARG would allow sufficient PAR formation in the presence of PARPi. We tested this hypothesis by measuring endogenous PAR levels in KB2P cells treated with the PARPi olaparib and the PARGi PDDX-004 (Figure 7.4A). To discriminate between stabilization of pre-existing and *de novo* synthesized PAR, we first incubated cells with the inhibitors for 1 hr and then exposed them to MMS to stimulate PARP activity. As predicted, olaparib treatment resulted in a strong reduction of PAR, already at nanomolar doses. Inhibition of PARG overcame this reduction and MMS treatment led to a further increase of the PAR signal. These data indicate that olaparib concentrations sufficient to kill cells do not completely inhibit PARP and that this residual activity is sufficient for PAR formation if PARG activity is suppressed. We conclude that endogenous PARG activity is required for efficient inhibition of PAR signaling by PARPi.

We next investigated the effect of different PARP family members on the PARPi response using BRCA-proficient KP3.33 cells, in which CRISPR/Cas9-mediated disruption of *Parp1*, *Parp2*, or *Parp3* was well tolerated (Figure S7.5A-C). While the PARPi sensitivity of *Parp2*$^{-/-}$ and *Parp3*$^{-/-}$ KP3.33 cells was significantly reduced by PARG inhibition, *Parp1* depletion resulted in partial resistance to olaparib (consistent with Murai *et al.*[7]), which was not further increased by PARGi treatment (Figure S7.5D). This result is in line with a previous report suggesting that up to 90% of cellular PAR results from PARP1 activity[31] and shows that PARG-related PARPi resistance is mainly mediated by PARP1 signaling.

7.4.6 PARG inhibition reduces PARP1-DNA complexes induced by PARPi treatment

It has been shown that PARP1 association to and dissociation from chromatin is regulated by its PARylation[5] and persistent PARP1-DNA complexes, induced by clinical PARPi, are toxic to cells[7]. We therefore measured the levels of chromatin-bound PARP1 in KB2P cells using a previously described trapping assay[7]. Immunoblot analysis showed olaparib-dependent accumulation of PARP1 in chromatin fractions, which was reduced in cells expressing PARG-targeting shRNAs (Figure 7.4B). Since stable PARG depletion could result in a substantial proportion of free PARP1 in a PARylated state, and therefore lower its affinity to chromatin, we repeated the PARP1 trapping assay in cells exposed to short-time inhibition of PARG (Figure 7.4C). Although single treatment with PDDX-004 led to decreased levels of chromatin-associated PARP1, simultaneous inhibition of both PARP1 and PARG resulted in PARP1 trapping comparable with olaparib alone. We further corroborated this finding by measuring PARP1 association kinetics at multi-photon laser-induced DNA damage

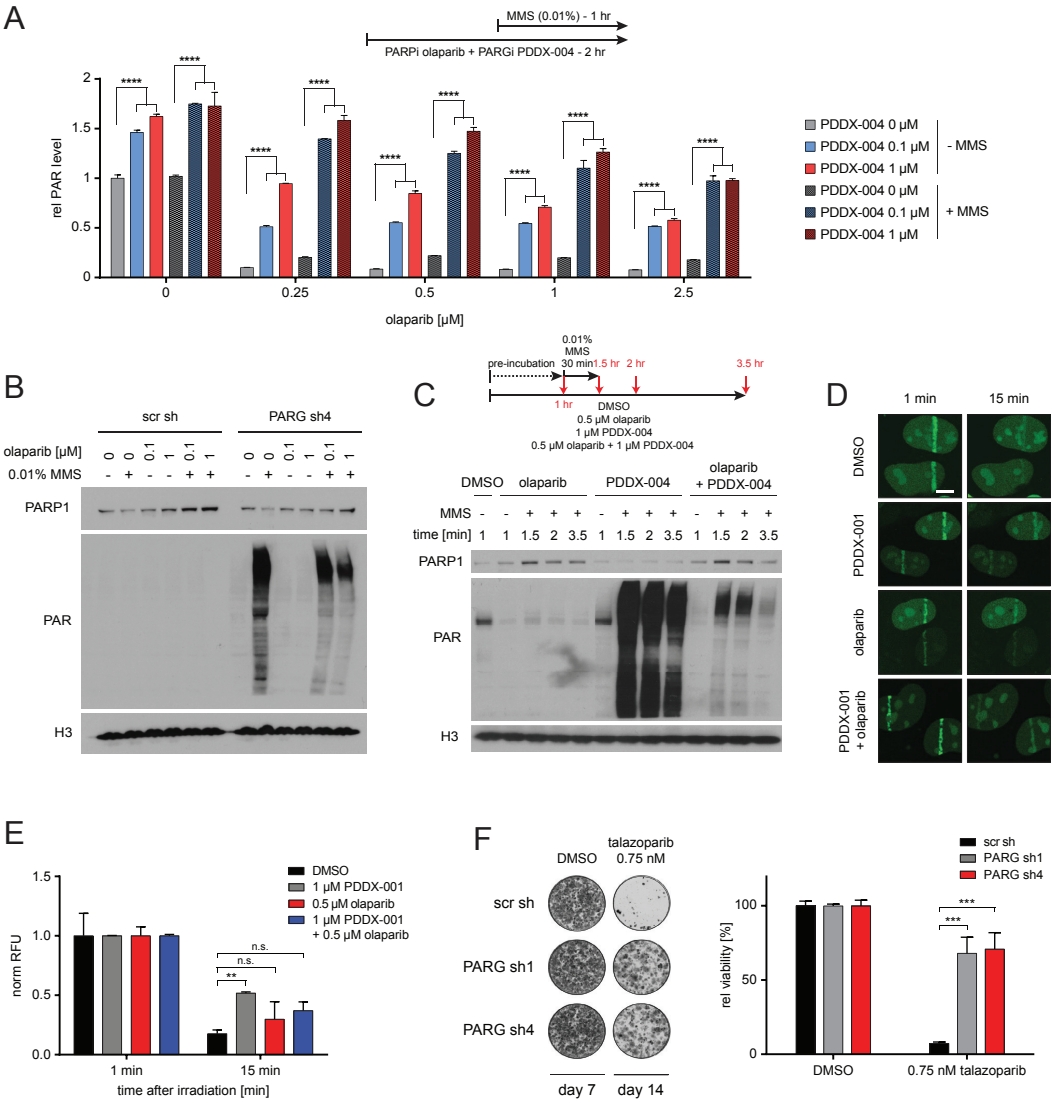

Fig. 7.4. PARG deficiency partially rescues PARylation and reduces the accumulation of PARP1-DNA complexes. (A) ELISA PAR assay in KB2P3.4 cells treated as indicated; data shown as mean ± SD of triplicate (t-test). $^{****}p < 0.0001$. **(B-C)** Immunoblot analysis of PARP1 in chromatin-bound fractions upon genetic (B) and chemical (C) inhibition of PARG in KB2P cells, treated as indicated; data representative for two independent experiments. **(D-E)** Representative images (left) and quantification (right) of analysis of PARP1 recruitment kinetics to multiphoton tracks in U2OS PARP1-GFP cells, following the indicated treatments. $^{**}p < 0.01$; n.s., not significant; two-tailed t-test, data represented as mean ± SEM. Scale bar, 10 μm. **(F)** Representative images of stained wells (right) and quantification (left) of clonogenic assay in KB2P cells expressing the indicated shRNAs and treated with talazoparib; data presented as mean ± SD of two experiments; $^{***}p < 0.001$ (two-tailed t-test). See also Figures S7.4 and S7.5.

sites in U2OS cells (Figure 7.4D-E). Cells were exposed to 0.5 μmol olaparib and/or the PARGi PDDX-001/PDD00017273 (1 μmol)[30], which alone efficiently inhibited downstream signaling of both proteins (Figure S7.5E-G). We utilized U2OS GFP-PARP1 cells and quantified the intensities of laser tracks; first, 1 min post irradiation, when under native conditions PARP1 accumulation reached a maximum, and then

15 min after the induction of DNA damage, when most of the chromatin had evicted PARP1 (Figure S7.5H). Both olaparib treatment alone and the combination with PDDX-001 resulted in a slight increase of chromatin-associated PARP1 15 min post irradiation (Figure 7.4D-E). Of note, even more PARP1 protein remained associated with damaged sites in cells exposed to PARGi only. The results, however, do not show any evidence that PARG depletion results in more rapid release of chromatin-bound PARP1. Taken together, our data demonstrate that PARG depletion does not enhance PARP1 dissociation from chromatin and therefore do not diminish PARP1 trapping *per se*. Instead, long-term suppression of PARG prevents excessive PARP1 binding and thus reduces PARPi-dependent accumulation of toxic PARP1-DNA complexes. The relevance of this finding is further supported by the fact that PARG depletion also results in resistance to talazoparib, a highly potent PARP1-DNA trapping agent in clinical use (Figure 7.4F).

7.4.7 PARG depletion alleviates PARPi-induced DNA damage

Following different forms of genotoxic stress, PARP1 activity has recently been shown to limit the rate of RF progression[32,33] by modulating fork reversal and preventing premature restart of reversed RF[34,35]. Deregulated RF remodeling by PARP inhibition was suggested to contribute to the synthetic lethality of PARPi with HR defects, as it increases the fraction of SSBs being processed into DSBs[36]. As shown in Figure 7.5A, we confirmed that PARPi treatment increases the DNA fiber track length upon induction of DNA damage with MMS or camptothecin (CPT). When PARG was also inhibited in these cells, the track length was significantly decreased, suggesting that PARG depletion prevents unrestrained RF progression in PARPi-treated cells (Figure 7.5A and Figure 7.5I). Concomitantly, PARG inhibition reduced the formation of DSBs in these cells, as measured by the neutral comet assay (Figure 7.5B and Figure 7.5J).

Given the role of PARP1 in DNA repair, we next investigated the PARP1-mediated recruitment of the scaffold protein XRCC1, a PAR interactor and a key player in the BER pathway[37]. To study the effects of PARPi and/or PARGi on XRCC1 recruitment, we applied the laser micro-irradiation assay to U2OS cells expressing a XRCC1-GFP fusion protein. We found that under drug-free conditions XRCC1-GFP was rapidly recruited to sites of laser-induced DNA damage (Figure 7.5C-D). Although a large proportion of the protein dissociated from chromatin within 60 min after irradiation, a substantial amount of XRCC1-GFP remained at the sites of DNA damage. In line with previous reports[38], treatment of cells with the PARPi olaparib abrogated XRCC1-GFP localization to laser-inflicted damage (Figure 7.5C-D). Inhibition of PARG mitigated the inhibitory effect of olaparib, however, and partially rescued XRCC1-GFP

recruitment. Importantly, the quantitative analysis of laser track intensities showed that the restored accumulation, although delayed in time, resulted in a similar retention of XRCC1-GFP at 1 hr post irradiation as in the control cells (Figure 7.5C-D). This effect of PARGi is specific to PARylation-induced recruitment of DNA repair factors, as we did not observe any differences in chromatin association of MDC1, which localizes to damaged sites in a PARP1-independent manner[39] (Figure 7.5E). As a readout for PARP1 function in the repair of SSBs, we employed the previously described Fast Micro-method SSB assay[40]. Consistent with our previous results, *Parg*-depleted cells exhibited increased capacity to repair SSBs in comparison with control cells (Figure 7.5F). This was further confirmed in cells exposed to olaparib for 24 hr. Immunofluorescence (IF) analysis of γH2AX foci revealed that *Parg*-depleted cells accumulated less olaparib-induced DNA damage (Figure 7.5G).

Based on our data, we conclude that PARG suppression not only reduces PARP1-DNA complexes but also rescues controlled RF progression and promotes the recruitment of DNA repair enzymes to sites of damage in cells exposed to PARPi. Altogether, this leads to a reduction of PARPi-induced DNA damage and improved PARPi survival (Figure 7.5H).

7.4.8 PARG deficiency overcomes PARPi toxicity in human cancer cells

The anticancer efficacy of PARPi has been validated in various clinical studies and several PARPi were recently approved for the treatment of patients with *BRCA1/2*-mutated tumors. We therefore determined whether PARG depletion confers PARPi resistance in human cancer cells by introducing two individual shRNAs targeting PARG in *BRCA1*-mutated SUM149PT (carrying a protein-truncating 2288delT mutation) and BRCA2-deficient DLD-1 cells. Both shRNAs efficiently suppressed PARG expression and conferred resistance to olaparib (Figure 7.6A-B and Figure S7.6A). Similarly, chemical inhibition of PARG led to increased survival of both cell lines in the presence of PARPi (Figure S7.6B-C).

Given that PARG loss causes PARPi resistance independently of BRCA1/2, we extended our analysis to a recently published pharmacogenomics dataset of 1,001 human cancer cell lines[41]. In particular, we assessed the correlation between half maximal inhibitory concentration (IC_{50}) values of PARPi and gene expression levels of 1,800 DDR-related factors (Table S7.2). Gene expression data and drug responses to four different PARPi (olaparib, veliparib, rucaparib, and talazoparib) were available for 935 cell lines from this panel. Statistical analysis revealed a significant negative association between PARG expression and IC_{50} values of all four PARPi (Figure 7.6C and Figure S7.6D); i.e., higher *PARG* RNA levels were related to in-

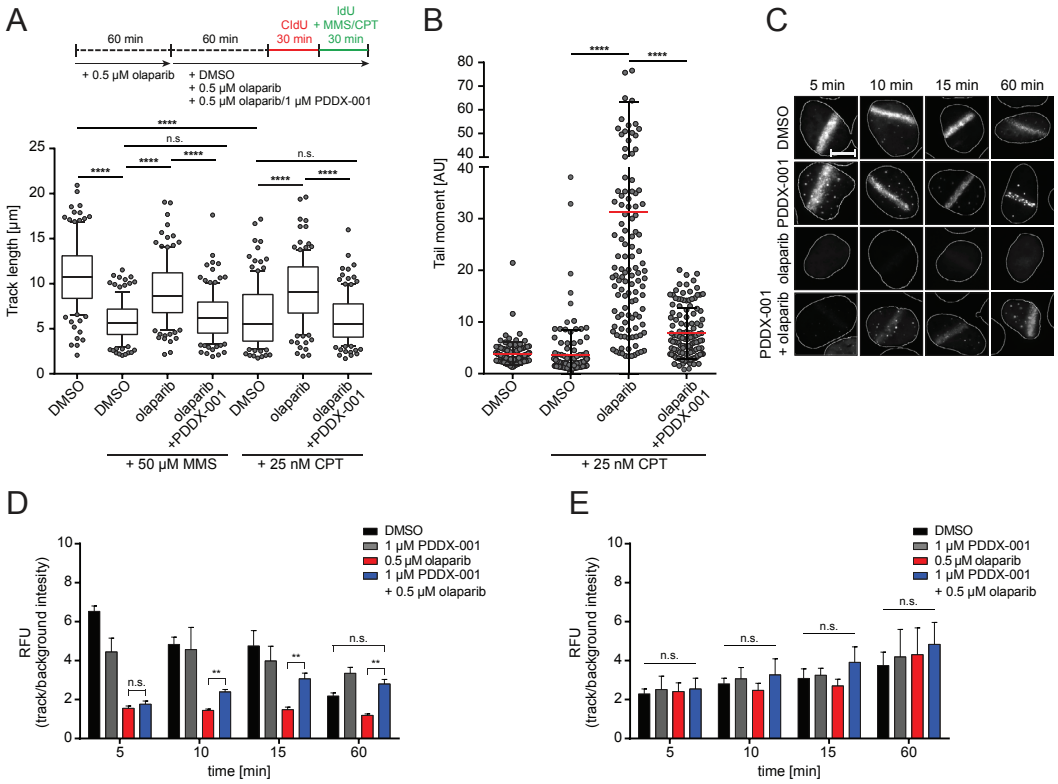

Fig. 7.5. PARG inhibition alleviates PARPi-induced DNA damage. (A) RF progression assay in U2OS cells exposed to indicated treatments; the experiment was repeated twice; box extends from 25$^{\text{th}}$ to 75$^{\text{th}}$ percentile, with a middle line representing the median and whiskers drawn down to the 10$^{\text{th}}$ percentile and up to the 90$^{\text{th}}$; Mann-Whitney U test; $^{****}p < 0.001$; n.s., not significant. **(B)** Neutral comet assay in U2OS cells treated as in (A); Mann-Whitney U test, $^{****}p < 0.001$, data shown as mean $\pm$ SD of a replicate; the experiment was repeated twice. **(C-D)** Representative images (C) and quantification (D) of time course analysis of GFP-XRCC1 recruitment in U2OS cells treated as indicated; $^{**}p < 0.01$; n.s., not significant; two-tailed unpaired t-test; data represent mean $\pm$ SEM of three independent experiments. Scale bar, 10 μm. **(E)** Quantification of MDC1 tracks following immunostaining; statistical analysis as in (D).

creased sensitivity to these drugs. A similar negative association was also observed for *PARP1* gene expression, in agreement with the concept that more PARP1 leads to more trapping of PARP1 onto DNA in the presence of PARPi.

7.4.9 PARG depletion occurs in triple-negative breast and serous ovarian cancer

To further assess the clinical relevance of PARG depletion, we measured the heterogeneity of PARG expression in large sections of 56 treatment-naive triple-negative human breast cancer (TNBC) biopsies from high-risk women eligible for PARPi treatment[42,43]. IHC analysis (Figure 7.6D-E, and Figure S7.6E) revealed that, although PARG protein was expressed in a vast majority of the biopsies, PARG-negative

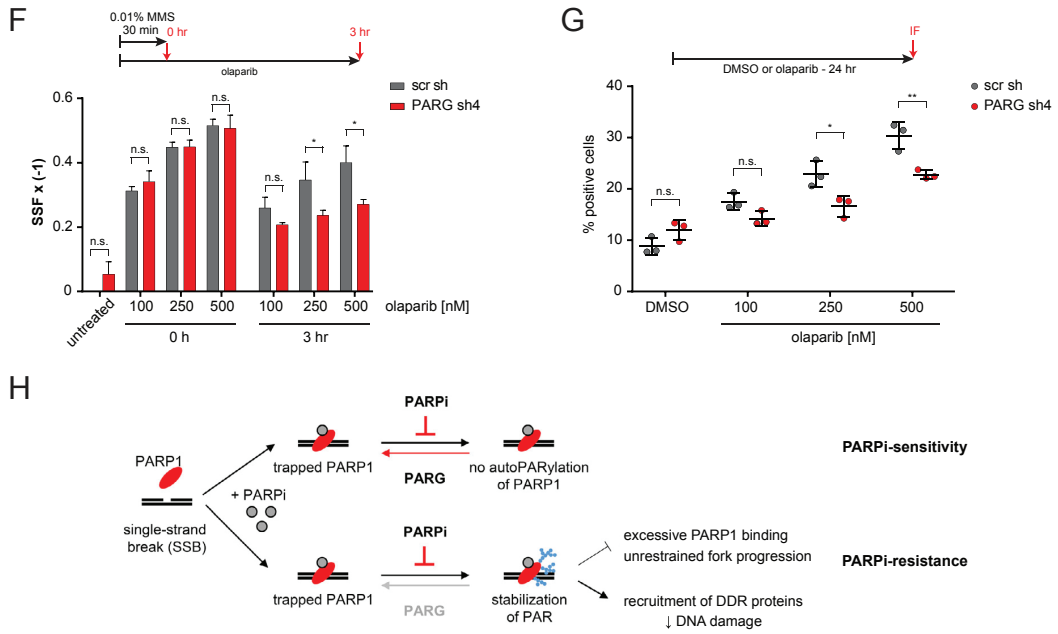

Fig. 7.5. **Continued. (F)** SSB assay in KB2P cells, treated as indicated; SSF, strand scission factor; data representative for two independent experiments, shown as mean ± SD of a replicate; two-tailed unpaired t-test; $^{*}p < 0.05$; n.s., not significant. **(G)** IF analysis of gH2AX foci in KB2P cells, treated as indicated; statistical analysis as in (F); $^{**}p < 0.01$; $^{*}p < 0.05$. **(H)** Proposed model: in the presence of PARPi, PARP1 maintains residual activity but is counteracted by PARG. Loss of PARG leads to stabilization of PAR chains and, consequently, limits accumulation of toxic PARP-DNA complexes, prevents unrestrained RF progression, and promotes the recruitment of the downstream factors. Together, this results in reduced PARPi-induced DNA damage and improves PARPi survival. See also Figure S7.5.

areas were found in a sizable proportion of samples. Specifically, 29 (52%) and 14 (25%) out of 56 cancers showed lack of PARG in areas corresponding to >10% and >20% of the tumor, respectively. Moreover, PARG-negative cells were positive for PAR, and in some of the samples PAR levels were substantially increased (Figure 7.6E). Of note, the variable degree of PAR could also reflect the degree of the endogenous DNA damage among the cases, as PARP enzymes are activated by DNA damage and these patients did not receive any genotoxic therapy. A similar PARG expression spectrum was also found in a cohort of serous ovarian carcinomas[44], a cancer type that has been recently approved for PARPi treatment (Figure 7.6D and Figure S7.6F). Taken together, our data show that PARG-depleted cells pre-exist in a substantial proportion of clinically relevant tumors and could potentially be selected by PARPi treatment.

7.4.10 PARG suppression results in acquired vulnerabilities

Molecular alterations that render cells resistant to targeted therapies may also cause synthetic dependencies, which in turn could be exploited therapeutically to prevent

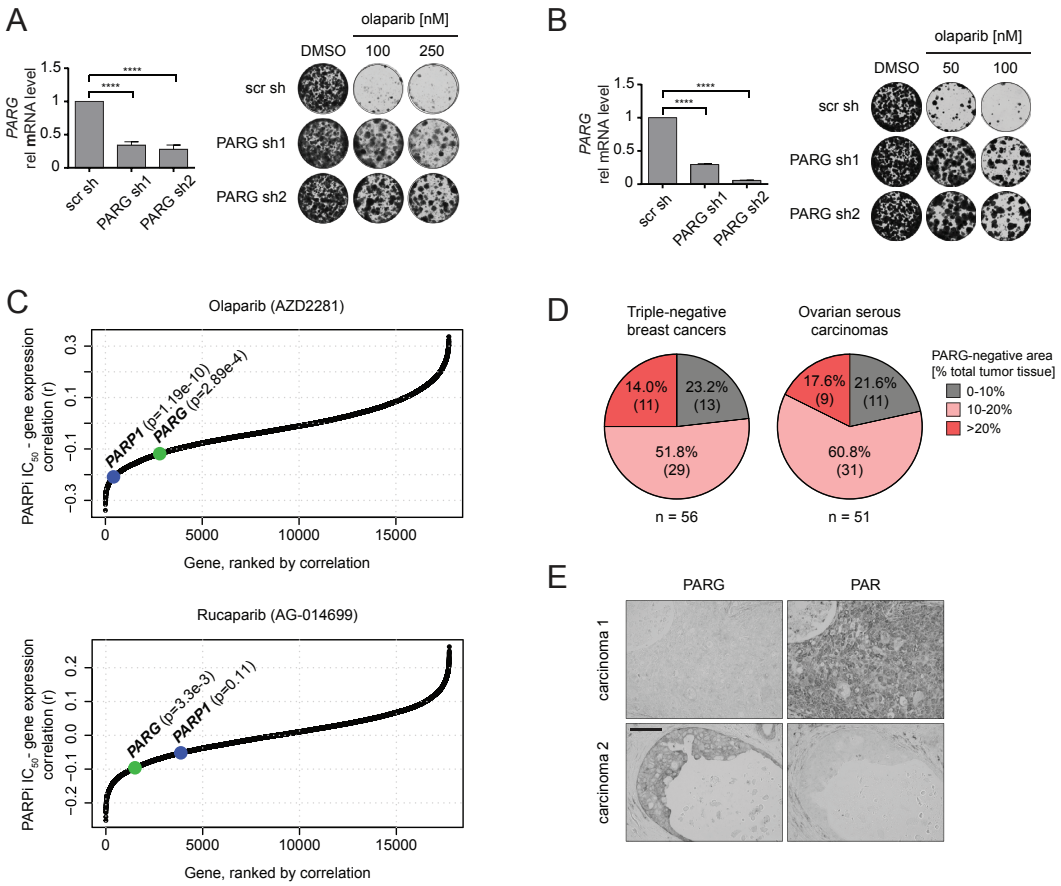

Fig. 7.6. PARG depletion in human cancer cells leads to PARPi resistance but results in acquired vulnerabilities. (A-B) Long-term clonogenic assay with SUM149PT (A) and DLD-1 BRCA2-deficient (B) cells expressing indicated shRNAs and treated with olaparib; PARG expression levels were determined by qRT-PCR (left; mean $\pm$ SD of triplicate, $^{****}p < 0.001$, t-test) and representative images of stained wells (right) are shown. **(C)** Correlation between IC_{50} of olaparib or rucaparib and expression of DDR genes; PARP1 and PARG are highlighted; p values were determined using the relation between estimated coefficient and Student's t distribution. **(D)** Summary of IHC analysis of PARG expression in TNBCs and ovarian serous carcinomas. **(E)** Representative images of PARG and PAR IHC of TNBC biopsies. Scale bar, 100 μm.

cancer progression. Perturbed PAR signaling due to downregulation of PARG has been shown to increase the sensitivity to IR[45]. Susceptibility to IR is also one of the characteristics of cells with dysfunctional BRCA1/2 proteins[46]. We therefore set out to determine whether PARG suppression could potentiate IR toxicity in *BRCA1/2*-mutated cells. For this purpose, SUM149PT cells with shRNA-mediated *PARG* knockdown were exposed to a range of IR doses and grown for another 7 days. Viability measures showed increased IR sensitivity of *PARG*-depleted cells in comparison with control populations (Figure 7.6F). Furthermore, dose-dependent sensitization was also achieved by chemical inhibition of PARG in SUM149PT, BRCA2-deficient DLD-1, and KB2P cells (Figure 7.6G-H and Figure S7.6G). Notably, we also observed synergistic effects between PARG inhibition and treatment with temozolo-

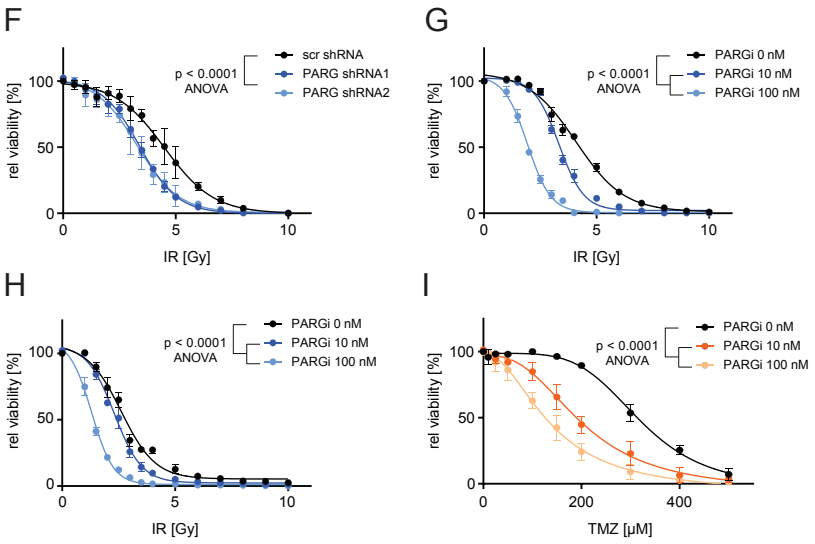

Fig. 7.6. **Continued. (F-G)** Response to irradiation of SUM149PT cells, expressing indicated shRNAs (F) or treated with PARGi (G). **(H)** Response to irradiation of DLD-1 BRCA2-deficient cells treated as indicated. **(I)** Response to temozolomide of SUM149PT cells treated as indicated. In (F)-(I) data are presented as mean ± SD of triplicates. See also Figure S7.6.

mide (Figure 7.6I and Figure S7.6H), an alkylating agent that has been previously shown to potentiate PARPi toxicity[8].

Together, these results illustrate that PARG suppression, although detrimental to PARPi efficacy, provides therapeutic vulnerabilities that could be used to target resistant tumors.

7.5 Discussion

In this study, we show that loss of PARG is a frequent mechanism of PARPi resistance in *Brca2*-mutated tumors. Our data provide an HR-independent mechanism for tumor cells to adapt their DDR in order to escape the lethal effects of PARPi. PARG is the main enzyme responsible for degrading nuclear PAR and thereby counteracting the action of PARP enzymes. Hence, PARG works in the same direction as PARPi and prevents PAR accumulation. Our finding that PARG depletion causes PARPi resistance in BRCA2-deficient tumors highlights an important aspect of PARPi therapy: the endogenous PARG activity in tumor cells is crucial for therapy success. As PARPi do not fully block PARP activity, loss of PARG activity is sufficient to restore PAR formation and rescue downstream signaling of PARP1.

Within the PARP family of ADP-ribosyltransferases, three family members, PARP1, PARP2, and PARP3, have been linked to DNA repair[47]. PARP1 is the most abundant

of these and has been shown to play critical roles in the DDR[48]. Upon DNA damage, RFs are rapidly and globally reversed and are maintained in the reversed state by transient PARP-mediated inhibitory ADP ribosylation of RECQ1 helicase, the enzymatic activity specifically required for restart of reversed RFs[34,35]. In this way, PARP1 represents a molecular switch to control transient fork reversal and RF restart following genotoxic stress[35]. Neelsen and Lopes[36] therefore suggested that the synthetic lethality of PARPi with HR defects results not only from an increasing load of SSBs but also from a greater fraction of these lesions being processed into DSBs. Whereas untreated cells gain extra time to repair DNA damage through RF reversal, PARPi-treated cells are unable to reverse forks efficiently, resulting in increased DNA breakage and the requirement for HR-mediated DSB repair. In line with this hypothesis, we found that PARG depletion restores controlled RF progression in the presence of PARPi and reduces subsequent DNA damage. We also found a mechanism at the level of DNA repair that contributes to PARPi resistance induced by PARG loss: PAR stabilization rescues the recruitment of the downstream scaffolding protein XRCC1, which is known to bring together a variety of components required for efficient SSB repair[49].

In BRCA-proficient tumors, the toxic effect of PARPi can also be counteracted by the loss of the drug target PARP1. Consistent with the data of Pettitt *et al.*[19], we found a significant enrichment for *Parp1*-targeting shRNAs in our drug resistance screen in BRCA-proficient mammary tumor cells. In accordance with the concept of synthetic lethality, however, this hit did not show up when we screened BRCA2-deficient mammary tumor cells. Previous screens in BRCA1-deficient tumor cells also did not yield *Parp1* as a hit[22].

Most PARPi do not only block the catalytic activity of PARP1 but also induce toxic PARP1-DNA complexes. Our study shows that PARG inhibition reduces the amount of trapped PARP1 by preventing its excessive binding. This result underscores the delicate balance between enzymatic PARP1 activity and its toxicity when trapped on DNA.

Since PAR synthesis and degradation go hand in hand in orchestrating the DNA damage response, the use of PARGi has been put forward for the treatment of cancers with DDR defects[50], and the possibility of a synthetic lethal interaction between PARG and BRCA proteins has received considerable interest. However, several studies that addressed this question have produced contradictory results[51–53], which suggest that sensitivity to PARG depletion may depend on the cell line and the degree of PARG suppression. Importantly, Koh *et al.*[54] showed that PARG depletion, although embryonically lethal, can be tolerated in embryonic stem cells cultured in the presence of PARPi. In our cell lines, both genetic depletion and chemical inhibition of PARG were well tolerated and did not affect cellular viability. Moreover,

homozygous loss of *Parg* was acquired *in vivo* in a substantial fraction of KB2P tumors.

PARG-negative clones were also found in a sizable proportion of human high-risk TNBCs or serous ovarian cancers, potential target groups for PARPi treatment due to the increased presence of HR-deficient cancers. Taken together, these data suggest that PARG-negative clones can be specifically selected by PARPi treatment and modulate therapy response.

While the clinical application of PARPi has initially focused on *BRCA1/2*-mutated tumors, the therapeutic scope of these drugs is now being extended to other molecular defects (reviewed by Lord and Ashworth[55]). Since PARG acts directly at PAR structures and independently of the HR pathway, stabilization of PARylation via PARG suppression might represent a generic mechanism of PARPi resistance, relevant for a broad spectrum of cancers. Although this is bad news for the clinical use of PARPi, loss of PARG can also be exploited as a potential Achilles' heel for cancer treatment, as it confers sensitivity to IR[45]. Our data indeed show that PARG suppression potentiates the toxicity of radiation therapy in BRCA-deficient cells. Additionally, we show that PARG inhibition synergizes with temozolomide, a chemotherapeutic agent that is now being evaluated in the clinic in combination with PARPi[56].

Our research has yielded a collection of matched PARPi-naive and -resistant *Brca2*$^{-/-}$ mouse mammary tumors, which can be further utilized in a search for additional resistance mechanisms. Although PARG loss was observed in the majority of the PARPi-resistant KB2P tumors, it cannot explain resistance in all cases. Three other candidates, *Rps6ka6*, *Socs4*, and *Pbrm1*, were validated as additional significant hits in a secondary screen. Since all three of these genes are connected to chromatin, it will be interesting to understand the underlying mechanism of how they affect PARPi response in a follow-up study.

In collaboration with the Durocher and Lord laboratories, we have recently identified that PARPi resistance can also be caused by loss of the Shieldin (SHLD) complex, which acts downstream of 53BP1 in blocking DNA end resection (Noordermeer *et al.*, manuscript submitted). Importantly, loss of the SHLD complex is not a generic PARPi resistance mechanism, since it causes PARPi resistance specifically in BRCA1- but not in BRCA2-deficient cells. In contrast, loss of PARG explains PARPi resistance in both *BRCA1*- and *BRCA2*-mutated tumors, as it operates independently of the HR pathway.

Taken together, our findings suggest that PARG is an important mediator of PARPi response. The presence of PARG-negative cells in treatment-naive tumors from the clinically relevant groups of high-risk women suggests that PARG loss should be

assessed as a potential cause of clinical PARPi resistance. In this case, measurement of PARG activity should further improve clinical decision making for patients with tumors that lack homology-directed DNA repair.

Author contributions Conceptualization, E.G., P.B., J.J., and S.R.; Methodology, E.G., A.A.D., W.W.W., D.I.J., and B.v.d.B.; Investigation, E.G., A.A.D., J.R.d.R., W.W.W., J.A.S., S.G.L., J. Bartkova, I.G., M.A.S., R.d.B., S.A., M.B., and A.K.; Software and Formal Analysis, E.G., J.R.d.R., R.d.B., and D.J.V.; Resources, D.I.J, D.J.O., and M.T.; Writing - Original Draft, Review & Editing - E.G., P.B., J.J., and S.R.; Supervision, M.v.d.V., M.v.V., L.F.A.W., J. Bartek., M.L., H.v.A., P.B., J.J., and S.R.; Funding Acquisition, D.J.O., J. Bartek., H.v.A., J.J., and S.R.

Acknowledgments We thank the members of the Preclinical Intervention Unit of the Mouse Clinic for Cancer and Ageing (MCCA) at the NKI, Wendy Sol, and Guotai Xu for their technical support with the animal studies, and we thank the NKI core facilities: Animal Pathology facility, Digital Microscopy facility, Genomics Core facility, and Animal facility for their excellent service. We are also grateful to Peter Bouwman (NKI) and Thanos Halazonetis (Geneve University) for help in generating the list of DDR-associated genes, to SurfSara for allowing us to use their HPC Cloud service for the computational analyses, and to Chief Pathologist Vera Timmermans Wielenga (Department of Pathology, Copenhagen University Hospital, Denmark) and the technician Maria Grønvig Nielsen (Danish Cancer Society Research Center) for their contribution to IHC analysis of TNBC biopsies. Financial support came from the Dutch Cancer Society (KWF 2011-5220 and 2014-6532), the Netherlands Organisation for Scientific Research (VICI 91814643 and a National Roadmap grant for Large-Scale Research Facilities), the Netherlands Genomics Initiative (93512009), Cancer Research UK (C480/A1141 and C5759/A17098), the Danish Cancer Society, Swedish Research Council, Cancerfonden and Danish National Research Foundation (project CARD), the Swiss National Science Foundation (310030_156869), the Swiss Cancer League (KLS-4282-08-2017), and the European Research Council (CoG-617485, CoG-681572, SyG-319661).

Conflict of interest The authors declare no potential conflicts of interest.

7.6 STAR Methods

7.6.1 Contact for reagent and resource sharing

Further information and requests for resources and reagents should be directed to and will be fulfilled by the Lead Contact, Sven Rottenberg (sven.rottenberg@vetsuisse.unibe.ch).

7.6.2 Experimental model and subject details

Mice All animal experiments were approved by the Animal Ethics Committee of The Netherlands Cancer Institute (Amsterdam, the Netherlands) and performed in accordance with the Dutch Act on Animal Experimentation (November 2014). *Brca2*$^{-/-}$*;p53*$^{-/-}$ mammary tumors were generated in *K14cre;Brca2*$^{F/F}$*;p53*$^{F/F}$ (KB2P) female mice, described previously[20]. Tumor implantation experiments were performed in syngeneic, wild-type F1 (first filial generation) FVB:129/Ola females, at the age of 6 weeks. Parental FVB (FVB/NRj) and 129/Ola animals were purchased from Janvier Labs and Harlan Olac, respectively, and crossed at the NKI Animal Facility. Animals were assigned randomly to the treatment groups and the treatments were supported by animal technicians who were blinded regarding the hypothesis of the treatment outcome. Collection of *Brca1*$^{-/-}$*;p53*$^{-/-}$ (KB1P) PARPi-naive and -resistant mouse mammary tumors was described before[24].

Human samples of triple-negative breast and serous ovarian cancer Retrospective Triple Negative Breast Cancer (TNBCs) biopsies from 56 clinical high-risk patients (high-risk definition according to the Danish Breast Cooperative Group; www.dbcg.dk accessed 22.10.2009) that underwent mastectomy between 2003 and 2015 were selected and classified as being triple negative according to the criteria set in the ASCO/CAP guidelines (ER $< 1\%$, PR $< 1\%$, HER2 0, 1+ or 2+ but FISH/ CISH negative). The patients presented a unifocal tumor of an estimated size of more than 20 mm. None of the patients had previous surgery to the breast and did not receive preoperative treatment[42,43]. This study was conducted in compliance with the Helsinki II Declaration and written informed consent was obtained from all participants and approved by the Copenhagen and Frederiksberg regional division of the Danish National Committee on Biomedical Research Ethics (KF 01-069/03).

Paraffin-embedded material from the cohort of ovarian tumors was collected at the Department of Pathology, University Hospital, Las Palmas, Gran Canaria, Spain, from surgical operations performed in the period 1995-2005. For the purpose of the present study, only samples from serous ovarian carcinoma (the type approved for

treatment by PARP inhibitors) were used from a larger cohort that was reported previously[44], and included also other histological types of ovarian tumors. The use of long-term stored tissue samples in this study was in accordance with the Spanish codes of conduct (Ley de Investigación Biomédica) and was approved by the review board of the participating institution. Patients were informed that samples may be used for research purposes under the premise of anonymity.

Cell lines All 2D cell lines used in this study were described previously: KB2P1.21, KB2P3.4, KP3.33[9], KB1P-G3[24], U2OS (RRID:CVCL_0042), SUM149PT (RRID:CVCL_3422), DLD-1 BRCA2(-/-) (Horizon Discovery, #HD 105-007; RRID:CVCL_HD57), HEK293FT (RRID:CVCL_6911).

For these lines, cell growth media were supplemented with 10 % (v/v) fetal calf serum (FCS, Sigma) and 50 units ml^{-1} penicillin-streptomycin (Gibco). KB2P1.21, KB2P3.4, KB1P-G3 and KP3.33 cells were grown in Dulbecco's Modified Eagle Medium/Nutrient Mixture F-12 (DMEM/F12; Gibco) containing 5 $\mu g\,ml^{-1}$ Insulin (Sigma, #I0516), 5 ng ml^{-1} cholera toxin (Sigma, #C8052) and 5 ng ml^{-1} murine epidermal growth-factor (EGF, Sigma, #E4127). U2OS cells were cultured in DMEM (Gibco) media supplemented with GlutaMAX (Gibco, #35050-061). SUM149PT cells were grown in RPMI1640 (Gibco) media, similarly to DLD-1 BRCA2(-/-) cells for which growth media was additionally enriched with 2 mmol L-glutamine and 25 mmol sodium bicarbonate. HEK293FT cells were cultured in Iscove's Modified Dulbecco's Media (IMDM, Gibco) supplemented with 2 mmol glutamine.

Tissue culture was carried out under standard conditions (37 °C, 5 % CO_2), except for KB2P1.21, KB2P3.4 and KB1P-G3 cells which were cultured under low oxygen conditions (3 % O2). All cell lines used in this study are of female origin, except for DLD-1 BRCA2(-/-) cells (male). Testing for mycoplasma contamination was performed on a regular basis.

Tumor-derived organoids KB2P26S.1, KB2P17 and KB2P12 tumor organoids were derived from a mammary KB2P PARPi-naive tumor (female donor), genotyped and cultured as described before[21]. Briefly, cultures were embedded in Culturex Reduced Growth Factor Basement Membrane Extract Type 2 (BME, Trevigen; 40 μl BME:growth media 1:1 drop in a single well of 24-well plate) and grown in Advanced DMEM/F12 (AdDMEM/F12, Gibco) supplemented with 1 mol HEPES (Sigma), GlutaMAX (Gibco) 50 units ml^{-1} penicillin-streptomycin (Gibco), B27 (Gibco), 125 mmol N-acetyl-L-cysteine (Sigma), 50 ng ml^{-1} murine epidermal growth factor (Sigma), 10 % (v/v) Rspo1-conditioned medium (kindly provided by Calvin Kuo, Stanford University) and 10 % (v/v) Noggin-conditioned medium[57]. Organoids were cultured

under standard conditions (37 °C, 5 % CO2) and regularly tested for mycoplasma contamination.

7.6.3 Method details

Generation of PARPi-naive and -resistant KB2P tumors

Spontaneous mammary tumors that arouse in KB2P (*K14cre;Brca2$^{F/F}$;p53$^{F/F}$*) mice were harvested, genotyped, sampled and cryopreserved (DMEM/F12, 10 % (v/v) FCS, antibiotics-free), as described before[20,58]. To obtain matched PARPi-naive and -resistant tumor panel, 21 individual spontaneous tumors were engrafted as tumor fragments in the fourth right mammary fat pad of wild-type FVB:129/Ola female mice (F1). Each tumor donor was transplanted into multiple animals (at least 2, 1 for control and 1 for PARPi treatment) and starting from 2 weeks after transplantation, tumor size was monitored at least three times a week. Tumor volume was determined by caliper measurements (length and width in mm) and calculated by using the following formula: $0.5 * \text{length} * \text{width}^2$. All treatments were initiated when tumors reached approx. 200 mm (100 % relative tumor volume). For PARPi treatment, AZD2461 powder was reconstituted in deionized water solution of 0.5 % (w/v) hydroxypropyl methylcellulose (HPMC) to a final concentration of 10 mg ml^{-1}. AZD2461 solution (100 mg kg^{-1}) or vehicle control (0.5 % HPMC) were administered to animals orally for 28 consecutive days. Upon tumor relapse to 100 % relative tumor volume, the treatment was repeated and continued for another 28 days, until acquired resistance. Animals were sacrificed when the tumors reached a volume of 1.500 mm. Tumor sampling included cryopreserved tumor pieces, fresh frozen tissue and formalin-fixed material (4 % (w/v) formaldehyde in PBS).

Generation of deep sequencing data and analysis

RNA preparation, sequencing and DIDS analysis Fresh-frozen tumor tissues were subjected to high-speed shaking in 2 ml microcentrifuge tubes containing 1 ml of TRIsure reagent (Bioline) and stainless steel beads (TissueLyser LT, Qiagen; 10 min, 50 Hz, room temperature). Homogenized lysates were further processed for RNA isolation following TRIsure manufacturer's protocol. Quality and quantity of the total RNA was assessed by the 2100 Bioanalyzer using a Nano chip (Agilent, Santa Clara, CA). Total RNA samples having RIN > 8 were subjected to library generation.

Strand-specific libraries were generated using the TruSeq Stranded mRNA sample preparation kit (Illumina Inc., San Diego, RS122-2101/2) according to the manufacturer's instructions (Illumina, Part #15031047 Rev. E). Briefly, polyadenylated RNA from intact total RNA was purified using oligo-dT beads. Following purification, the

RNA was fragmented, random primed and reverse transcribed using SuperScript II Reverse Transcriptase (Invitrogen, part #18064-014) with the addition of Actinomycin D. Second strand synthesis was performed using Polymerase I and RNaseH with replacement of dTTP for dUTP. The generated cDNA fragments were 30 end adenylated and ligated to Illumina Paired-end sequencing adapters and subsequently amplified by 12 cycles of PCR. The libraries were analyzed on a 2100 Bioanalyzer using a 7500 chip (Agilent, Santa Clara, CA), diluted and pooled equimolar into a 10 nmol sequencing stock solution.

Illumina TruSeq mRNA libraries were sequenced with 50 base single reads on a HiSeq2000 using V3 chemistry (Illumina Inc., San Diego). The resulting reads were trimmed using Cutadapt[59] (version 1.12) to remove any remaining adapter sequences, filtering reads shorter than 30 bp after trimming to ensure good mappability. The trimmed reads were aligned to the GRCm38 reference genome using STAR[60] (version 2.5.2b). QC statistics from Fastqc[61] (version 0.11.5) and the abovementioned tools were collected and summarized using Multiqc[62]. Gene expression counts were generated by featureCounts[63] (version 1.5.0-post3) using gene definitions from Ensembl GRCm38 version 76. Normalized expression values were obtained by correcting for differences in sequencing depth between samples using DESeq's median-of-ratios approach[64] and then log-transforming the normalized counts. Differentially expressed genes were identified using DIDS[27], using a threshold of $p < 0.05$ for statistical significance. Given that generated p value was a very conservative estimate of the true p value and was only used as a heuristic filter, we did not apply multiple testing correction (in accordance with de Ronde *et al.*[27]). Selected genes were subsequently ranked by the number of (resistant) samples that were considered to show differential expression according to the DIDS criteria.

Genomic DNA extraction and CNV sequencing Genomic DNA was isolated from fresh-frozen tumor material using standard phenol:chloroform extraction. CNV-Seq was performed using double stranded DNA (dsDNA), quantified with the QubitO®dsDNA HS Assay Kit (Invitrogen, #Q32851). To obtain fragment sizes of 160-180 bp, 2μg of dsDNA were fragmented by Covaris shearing and purified using 1.8X Agencourt AMPure XP PCR Purfication beads according to manufacturer's protocol (Beckman Coulter, #A63881). Next, sheared DNA was quantified and qualified on a BioAnalyzer system with the DNA7500 assay kit (Agilent Technologies, #5067-1506). Library preparation for Illumina sequencing was carried out with 1μg of DNA and KAPA HTP Library Preparation Kit (KAPA Biosystems, #KK8234). To obtain a sufficient yield for sequencing, 4-6 PCR cycles were performed during the library enrichment step. Prepared libraries were cleaned up using 1X AMPure XP beads and analyzed on a BioAnalyzer system using the DNA7500 chips to determine the molarity. Finally, up to 11 uniquely indexed samples were

pooled (equimolar pooling) in a final concentration of 10 nmol and sequenced on an Illlumina HiSeq2500 machine in one lane of a single read 65 bp run, according to manufacturer's instructions. The resulting reads were trimmed using Cutadapt[59] (version 1.12) to ensure a uniform length of 50 bp reads between samples and to remove any remaining adapter sequences. After trimming, reads shorter than 30 bp were removed to ensure good mappability. The trimmed reads were aligned to the GRCm38 reference genome using BWA aln[65] (version 0.7.15). The resulting alignmentswere sorted and marked for duplicates using Picard tools (version 2.5.0). QC statistics from Fastqc[61], Samtools[66] (version 1.2) and the above-mentioned tools were collected and summarized using Multiqc[62]. Copy number calls were generated using the QDNAseq[67] and QDNAseq.mm10 packages from Bioconductor (versions 1.8.0 and 1.4.0, respectively). To select for acquired copy number events, the CNV calls from resistant samples were filtered to remove any calls that were already present in the matched sensitive sample. After this filtering, genes were ranked by their recurrence (number of resistant samples with a loss/gain), dropping any genes that were only aberrant in a single sample.

DDR-related gene list The DDR gene set was generated based on the gene list from Thanos Halazonetis (Geneve University) and the NCBI search (terms: 'DNA repair', 'DNA damage response', 'DNA replication', 'telomere-associated genes'). See Table S7.2 for the complete gene list.

Final ranking of gene candidates To obtain a final ranking for the 82 candidate genes, we first created two new DIDS and CNV rankings, containing only these candidate genes. Next, to prioritize candidates with a strong correlation between copy number and expression, we created a third ranking by calculating the spearman correlation between the copy number values and expression of each gene across all samples, and sorting the genes by decreasing correlation. These three ranks were aggregated using the R package RobustRankAggreg[68] (version 1.1) to obtain the final rankings using three different aggregation methods (Stuart, RRA and Mean). To handle ties within the DIDS/CNV ranks (due to the discrete nature of these ranks), genes with the same values in these ranks were assigned the same rank value before the aggregation.

Immunohistochemistry analysis

PARG IHC analysis in KB2P tumor panel Immunohistochemical staining was performed on formalin-fixed paraffin embedded (FFPE) material of the KB2P tumor panel. First, antigen retrieval was performed by cooking the samples in citrate buffer 6.0 pH (ScyTek Laboratories) for 15 min in pressure cooker (110 °C).

Next, endogenous peroxidase activity was blocked by incubation a with methanol solution of 3 % (v/v) H_2O_2 for 20 min. 10 % (v/v) milk solution in PBS was used as a blocking buffer (30 min, room temperature) and PBS containing 1 % (w/v) bovine serum albumin and 1.25 % (v/v) normal goat serum was used as antibody diluent. Incubation with primary PARG antibody (Thermo Fisher Scientific; #PA5-14158; diluted 1:100, final concentration 20 $\mu g\,ml^{-1}$) was carried out overnight at 4 °C and followed by 30 min incubation with secondary Goat-a-Rabbit-Bio antibody (DAKO, #E0432; 1:1000) at room temperature. For detection, samples were exposed to PBS solution containing DAB substrate (Sigma, #D5905) and 0.025 % (v/v) H_2O_2 (Sigma, #A31642) for 20 min and hematoxylin counterstaining. Semi-quantitative (scoring: 1-low signal, 2-high signal) PARG expression analysis was carried out by a pathologist who was blinded regarding the identity of the samples.

PARG/PAR analysis in TNBC and serous ovarian carcinoma cohorts Five-mm tissue sections were cut from the formalin-fixed, paraffin-embedded tissue blocks and mounted on Super Frost Plus slides (Menzel-Gläser, Braunschweig, Germany), baked at 60 °C for 60 min, deparaffinized, and rehydrated through graded alcohol rinses. Heat induced antigen retrieval was performed by immersing the slides in citrate pH 6.0 buffer and heating them in a 750 W microwave oven for 15 min followed by immunohistochemistry staining with the primary antibodies as follows: anti-PARG antibody from Thermo Scientific (PA5 14158; diluted 1:2000) and anti-PAR antibody from GeneTex (10H, GTX75054, diluted 1:2500. The sections were incubated with the primary antibodies overnight in a cold-room, followed by subsequent processing by the indirect streptavidin-biotin-peroxidase method using the Vectastain Elite kit (Vector Laboratories, Burlingame, CA, USA) and nickel-sulphate-based chromogen enhancement detection as previously described[69], without nuclear counterstaining. For negative controls, sections were incubated with non-immune sera. The results were evaluated by two experienced researchers, including a senior oncopathologist, and the data expressed as percentage of positive tumor cells within each lesion.

Constructs, lentiviral transductions and genome editing

Constructs A collection of 1,976 lentiviral hairpins targeting 391 DDR-related mouse genes (pLKO.1; DDR library) were derived from the Sigma Mission library (TRCMm1.0) as described before[22]. Custom-made shRNA library (pLKO.1) targeting 82 candidate genes (identified by the multi-omics analysis of KB2P tumors) and 32 non-essential genes (552 shRNAs in total, on average 5 shRNAs/gene) was obtained from the Sigma Mission collection (TRCMm1.0) (see also Table S7.4). Non-essential genes were used as negative controls for the enrichment analysis, and were selected based on the work of Hart and colleagues[70] and RNA-Seq data from KB2P tumors (non-expressed genes).

Individual hairpin constructs used in the validation studies were selected from the TRC library: mouse PARG - sh1: TRCN0000126559, sh4: TRCN0000126562; human PARG - sh1: TRCN0000051303, sh2: TRCN0000051305) (see also Table S7.6). For CRISPR/Cas9-based genome editing two different systems were used: (1) for targeting *Parg* locus (Figure 7.3D and Figure S7.3D-F) the Cas9 expressing pGSC_Cas9_Neo vector (kind gift from Bastiaan Evers, NKI) was used and individual gRNAs (see Table S7.6) were cloned into the iKRUNC-Puro system described previously[71]; (2) for targeting *Parp1*, *Parp2*, *Parp3* loci (Figure S7.5A-D) lentiCRISPRv2 vector was used and individual gRNAs (see Table S7.6) were cloned as described previously[72]. For laser micro-irradiation experiments, pEGFP-C1-XRCC1 (gift from Simon Bekker-Jensen) and pEGFP-c3-PARP1 (gift from Valerie Schreiber) vectors were used. pEGFP-N1-CHD2 vector has been described before[73]. All constructs were verified by Sanger sequencing.

Lentiviral transductions Lentiviral stocks, pseudotyped with the VSV-G envelope, were generated by transient transfection of HEK293FT cells, as described before[74]. Lentiviral titers were determined using the qPCR Lentivirus Titration Kit (Applied Biological Materials), following the manufacturer's instructions. For all experiments the amount of lentiviral supernatant used was calculated to achieve the MOI (multiplicity of infection) of 50, except for the transduction of the lentiviral library (genetic screens) for which an MOI of 1.5 was used. To ensure efficient transduction, cells were incubated with lentiviral supernatants overnight in the presence of polybrene ($8\,\mu g\,ml^{-1}$). Antibiotic selection was initiated 24 hr post-transduction and was carried out for 5 consecutive days. Tumor-derived organoids were transduced according to a previously established protocol[21].

Genome editing For CRISPR/Cas9-mediated genome editing with the iKRUNC system, KB2P1.21 or KB2P3.4 cells were first transduced with the lentiviral pGS-Cas9 (Neo) construct (MOI 50) and grown under G418 selection ($500\,\mu g\,ml^{-1}$) for 5 days. Next, neomycin-selected cells were incubated with lentiviral supernatants of iKRUNC-Puro vectors (gRNA-encoding constructs, MOI 50) and exposed to $3\,\mu g\,ml^{-1}$ puromycin for 5 days. To induce gRNA expression, puromycin-surviving cells were treated for another 5 days with $3\,\mu g\,ml^{-1}$ doxycycline (Sigma). For CRISPR/Cas9-mediated genome editing with lentiCRISPRv2 system, KP3.33 cells were transduced with the lentiviral supernatant (MOI 50) and grown under Puromycin ($3\,\mu g\,ml^{-1}$) selection for 5 days. To assess the modification rate, genomic DNA was extracted (Puregene Core Kit A, Qiagen) and $100\,\mu g$ was used as an input for the PCR amplification of the targeted sequence. PCR reaction was performed with Thermo Scientific Phusion High-Fidelity PCR Master Mix (Thermo Scientific), according to manufacturer's instructions (3-step protocol: annealing - 60 °C for 5 s, extension time 15 s) and using primers listed in Table S7.6. Resulting PCR products were

purified using the MinElute PCR Purification Kit (Qiagen) and eluted in 50 μl of water. Finally, 2 μl of purified DNA served as a template for the BigDye Terminator v3.1 reaction (Thermo Fisher). BigDye PCR reactions were performed with the same forward primers as in the preceding PCR reactions (no reverse primer used) and according to the BigDye manufacturer's protocol. Allele composition was determined with the TIDE analysis[29] by comparing sequences from modified and parental (non-transduced control) cells.

Functional genetic screens

The DDR shRNA library and the shRNA library targeting candidate genes (secondary screen) were stably introduced into 2D lines (KP3.33, KB2P1.21, KB2P3.4) and organoids (ORG-KB2P26S.1) by lentiviral transduction (MOI 1.5). After antibiotic selection (puromycin, 3 μl ml^{-1}, 5 days) cells were seeded for the clonogenic assay with PARPi or pelleted for the genomic DNA isolation (day 0; control samples for the enrichment analysis). The total number of cells used in a single screen was calculated as following: library complexity $*$ coverage (1000x). Cells were seeded at low confluency to avoid contact inhibition between single clones (2D cells - 30,000 cells per 10 cm dish; organoids - 50,000 cells/well, 24-well format) and in the presence of PARPi (KB2P1.21/KB2P3.4: 200 nmol olaparib, 300 nmol AZD2461; KP3.33: olaparib 10 μmol; ORG-KB2P26S.1: 25 nmol AZD2461). Cells were selected with PARPi for 3 weeks, and media was refreshed at least twice per week. PARPi-surviving clones were pooled and genomic DNA was extracted (QIAmp DNA Mini Kit, Qiagen). shRNA sequences were retrieved by a two-step PCR amplification, as described before[22]. To maintain screening coverage, the amount of genomic DNA used as an input for the first PCR reaction was taken into account (6 μg of genomic DNA per 106 genomes, 1 μg per PCR reaction). Resulting PCR products were purified using MinElute PCR Purification Kit (Qiagen) and submitted for Illumina sequencing. Sequence alignment and enrichment analysis (day 0 vs PARPi-treated population) was carried out using MaGECK software[23].

Long-term clonogenic assays

Long-term clonogenic assays were performed in 6-well (KB2P1.21, KB2P3.4, KB1P-G3, KP3.33) or 12-well plates (SUM149PT, DLD-1 BRCA2(-/-)). Cells were seeded at low density to avoid contact inhibition between the clones (KB2P1.21 - 3,000 cells/well, KB2P3.4 and KP3.33 - 2,000 cells/well, KB1P-G3 - 5,000 cells/well, SUM149PT and DLD-1 BRCA2(-/-) - 3,000 cells/well) and cultured for 2 weeks, except for control (DMSO-treated) KB2P1.21, KB2P3.4, KB1P-G3 and KP3.33 cells, which were stopped after 7 days. Media was refreshed at least twice a week. For the quantification, cells were incubated with Cell-Titer Blue (Promega) reagent and later fixed with 2 % formaldehyde and stained with 0.1 % crystal violet. Clonogenic assays

with cells with CRISPR/Cas9-based genome editing were quantified with TIDE, similarly to a previously described method[75]. Drug treatments: cells were grown in the continuous presence of temozolomide, PARPi (olaparib, talazoparib or AZD2461), and/or PARGi (PDDX-004), at the indicated concentrations. All compounds were reconstituted in DMSO (PARP/PARG inhibitors: 10 mmol, temozolomide: 5 mg ml^{-1}). For the ioninizing irradiation studies, cells received single irradiation doses 24 hr after seeding. IR treatments were carried out using Gammacell 40 Extractor (Best Theratronics Ltd.).

RT-qPCR

To determine gene expression levels, total RNA was extracted from cultured cells using ISOLATE II RNA Mini Kit (Bioline) and used as a template to generate cDNA with Tetro cDNA Synthesis Kit (Bioline; oligo $(dT)_{18}$ mix). Quantitative RT-PCR was performed using SensiMix SYBR Low-ROX Kit (Bioline; annealing temperature - 60 °C) in a Lightcycler 480 384-well plate (Roche), and analyzed using Lightcycler 480 Software v1.5 (Roche). Mouse *Hrtp* and human *HPRT* were used as housekeeping genes (control). The primer sequences used in this study are listed in Table S7.6.

PAR immunoblotting

Tumor-derived organoids or 2D cells were washed with PBS, trypsinized and then lysed for 30 min in RIPA buffer supplemented with protease inhibitors (cOmplete Mini EDTA-free, Roche) and 1 μmol PARG inhibitor ADP-HPD (Merck). The protein concentration was determined using Pierce BCA Protein Assay Kit (Thermo Scientific). SDS-Page was carried out with the Invitrogen NuPAGE SDS-PAGE Gel System (Thermo Fisher; gel: 4 % to 12 % Bis-Tris, buffer: MOPS, input: 50 μg protein), according to the manufacturer's protocol. Next, proteins were electrophoretically transferred to a nitrocellulose membrane (Biorad) and then the membrane was blocked in 5 % (w/v) milk (PAR) solution in Tris-buffered saline Triton X-100 buffer (TBS-T; 100 mmol Tris, 7.4 pH, 500 mmol NaCl, 0.1 % (v/v) Triton X-100). Membranes were incubated overnight with primary antibodies in blocking buffer, at 4 °C. Horseradish peroxidase (HRP)-conjugated secondary antibody incubation was performed for 1 hr at room temperature in blocking buffer and signals were visualized by ECL (Pierce ECL Western Blotting Substrate, Thermo Scientific). Primary antibodies used in this study: mouse monoclonal anti-PAR (H10) (Millipore), 1:1000; rabbit polyclonal anti-PARP1 (#9542, Cell Signaling), 1:1000; rabbit polyclonal anti-PARP3 (#ALX-210-541- R100, Enzo Life Sciences), 1:500; rabbit polyclonal anti-Histone H3 (#ab1791, Abcam), 1:5000; mouse monoclonal anti-GADPH (6C5) antibody (Santa Cruz), 1:5000 dilution. Secondary antibody used in this study: rabbit polyclonal anti-mouse immunoglobulins/HRP (Dako), diluted 1:5000.

PARP1 trapping assay

The PARP1 trapping assay was adapted from Murai *et al.*[7]. In brief, 24 hr prior the assay, KB2P cells were seeded on 10 cm dishes to achieve ~90 % confluency. Drug treatments: (1) KB2P cells with genetic depletion of PARG (Figure 7.4B) were treated with olaparib (0, 0.1 or 1 μmol) and 0.01 % MMS for 2 hr; (2) KB2P cells with chemical inhibition of PARG (time-course experiment, Figure 7.4C) were first pre-incubated with 0.5 μmol olaparib and/or1 μmol PDDX-004 for 1 hr, and then exposed to the same treatments but in a presence of 0.01 % MMS for 30 min; following incubation with MMS cells were further incubated with olaparib and/or PDDX-004 for 0.5 or 2 hr, as shown on Figure 7.4C. After indicated treatments cells were trypsinized and subsequently lysed to isolate chromatin-bound fractions. Fractionation was performed with Subcellular Protein Fractionation Kit from Thermo Scientific (#78840, Rockford, IL, USA), following the manufacturer's instructions and in the presence of 1 mM of PARGi ADP-HPD (#118415, Calbiochem) in the lysis buffers. Immunoblotting was carried out as described in previous section (Immunoblotting). Experiments were repeated three times.

PARG activity assay

Enzymatic activity of endogenous PARG was measured using HT Colorimetric PARG Assay Kit (#4683-096-K, Trevigen), following the manufacturer's instructions. Experiments were repeated three times.

PAR ELISA assay

To measure endogenous PAR levels cells were seeded on 6-well plate 24 hr prior to PARPi, PARGi or combined PARPi/PARGi treatment to achieve ~90 % confluency at the day of the assay. Cells were treated with different doses of inhibitors for 2 hr, and additionally some of the samples were exposed to 0.01 % MMS for the last 60 min. Cell lysis, protein isolation and PAR ELISA were carried out using HT PARP In Vivo Pharmacodynamic Assay II kit (#4520-096-K, Trevigen), according to the manufacturer's protocol. Protein concentration was measured with Pierce BCA Protein Assay kit (Thermo Scientific).

PAR immunofluorescence analysis

PAR levels were measured using the adapted immunofluorescent PAR cell assay described before[76]. Briefly, cells were seeded on Corning 96-well special optics plates (#CLS3720, Sigma) 24 hr prior the assay to achieve ~90 % confluency. Next, cells were treated with a range of PARGi doses for 2 hr, and for the last 60 min cells were additionally exposed to 0.01 % MMS. After incubation with drugs, plates

were fixed with ice-cold 95 % (v/v) methanol/PBS (100 ml/well) for 15 min at −20 °C. Plates were then washed twice with PBS and cells were permeabilized by adding 100 μl per well of 0.1 % (v/v) Triton X-100 in PBS and incubating for 20 min at room temperature. Incubation with the primary mouse monoclonal anti-PAR (H10) antibody (Millipore), diluted 1:4000 in PBS solution containing 5 % (v/v) FBS and 0.05 % (v/v) Tween-20, was carried out overnight at 4 °C. After three washes with PBS, cells were incubated for 1 hr (room temperature) with polyclonal AlexaFluor488 goat anti-mouse immunoglobulins (1:1000) and Hoechst (1:5000; Thermo Scientific) diluted in 5 % (v/v) FBS/0.1 % (v/v) Triton X-100 in PBS. PAR immunofluorescent signal was detected with a Leica TCS SP8 confocal system (Leica Microsystems), using a HC PL APO 40x/1.10 W objective. Total nuclear intensities were measured per nuclei with ImageJ software. For each well, four different areas (200 cells on average) were imaged and analyzed. Each experiment was repeated three times.

RAD51/53BP1 IRIF analysis

Cultured cells Cells were seeded on Millicell EZ slides (#PEZGS0816, Millipore) 24 hr prior the assay to achieve ∼90 % confluency. Cells were then irradiated using the Gammacell 40 Extractor (Best Theratronics Ltd.) at the dose of 10 Gy and allowed to recover for 4 hr. Next, cells were fixed with 4 % (w/v) solution of formaldehyde in PBS for 30 min and permeabilized in 0.2 % (v/v) Triton X-100 in PBS^{++} (PBS solution containing 1 mmol $CaCl_2$ and 0.5 mmol $MgCl_2$) for 20 min. To minimize the background, cells were further incubated for 30 min in staining buffer (1 % (w/v) BSA, 0.15 % (w/v) glycine and 0.1 % (v/v) Triton X-100 in PBS^{++}). Staining buffer was also used as a solvent for antibodies - primary antibodies: rabbit anti-RAD51 (gift from Roland Kanaar, Erasmus MC, Rotterdam), diluted 1:5000, rabbit polyclonal anti-53BP1 (Abcam), diluted 1:1000, secondary antibody - goat polyclonal anti-rabbit, Alexa FluorO®658-conjugated, diluted 1:1000. Incubation with primary and secondary antibodies was done for 2 hr and 1 hr, respectively. All incubations were performed at room temperature. Samples were mounted with VECTASHIELD Hard Set Mounting Media with DAPI (#H-1500; Vector Laboratories). Images were captured with Leica SP5 (Leica Microsystems) confocal system and analyzed using an in-house developed macro to automatically and objectively evaluate the DNA damage-induced foci[22]. Fraction of positive cells was determined for each sample using following criteria: RAD51 > 5 foci/nucleus, 53BP1 > 10 foci/nucleus. Experiment was performed in triplicate (on average 100 cells/replicate). As a positive control for RAD51 staining, BRCA-proficient KP3.33 cells were used.

***In situ* analysis of GEMM tumors** Matched PARPi-naive and -resistant KB2P tumors, and KP (*K14cre;p53$^{F/F}$*) tumor (positive control) were re-transplanted into wild-type

syngeneic mice. Upon tumor outgrowth to 500 mm tumors were locally irradiated (dose: 15 Gy) using CT-guided high precision cone beam micro-irradiator (X-RAD 225Cx) or left untreated (control). Two hr post-irradiation tumors were isolated and fixed in 4 % (w/v) solution of formaldehyde in PBS. FFPE material was then used for immunofluorescent staining. First, samples were deparaffinized and antigen retrieval was done by cooking samples in DAKO Target Retrieval Solution pH 9 (#S236784, DAKO) for 20 min in microwave at ~600 W. Next, samples were permeabilized in 0.2 % (v/v) Triton X-100 in PBS for 20 min and further incubated with DNase (1000 u ml^{-1}; #04536282001, Roche) in humidified chamber for 1 hr at 37 °C. Incubation with antibodies, mounting, imaging and analysis were carried out as described for cultured cells. At least five different areas were imaged and analyzed for each sample. All incubations were performed at room temperature, unless otherwise stated.

Immunofluorescent staining of Olaparib-Induced γH2AX foci Cells were seeded on Corning 96-well special optics plates (#CLS3720, Sigma) 24 hr prior the olaparib treatment to achieve ~60 %. Next, cells were incubated with olaparib for the next 24 hr and subsequently fixed and stained following the same protocol as described for RAD51/53BP1 IRIF assay (cultured cells). Primary antibody used in this assay: Phospho-Histone H2A.X (Ser139) rabbit monoclonal antibody, Cell Signaling, #2577 (1:200 in staining buffer). Immunofluorescent signal was detected with a Leica TCS SP8 confocal system (Leica Microsystems), using a HC PL APO 40x/1.10 W objective. Foci were quantified using in-house developed macro to automatically and objectively evaluate the DNA damage-induced foci[22]. For each condition, four different areas (200 cells on average) were imaged and analyzed. Experiment was performed in triplicate and repeated twice.

DNA fiber assay

Replication fork progression assay Fork progression was measured using an adapted method described previously in Zellweger *et al.*[35]. Briefly, asynchronously growing U2OS cells were first incubated with 0.5 μmol PARPi (olaparib or AZD2461) for 1 hr and further treated with 0.5 μmol PARPi alone, or in combination with 1 μmol PDDX-001, for another 60 min. Next, cells were labeled with 30 μmol CIdU (Sigma-Aldrich) for 30 min, washed twice with PBS, and labeled with 250 μmol IdU in the presence of genotoxic agents - 50 μmol MMS or 25 nmol CPT for another 30 min. Following pulse labelling, cells were quickly trypsinized and resuspended in PBS at $2.5 * 10^5$ cells per ml. Next, labeled cells were diluted 1:8 with unlabeled cells, and 2.5 ml of cells were mixed with 7.5 ml of lysis buffer (200 mmol Tris-HCl, 7.5 pH, 50 mmol EDTA, and 0.5 % (w/v) SDS) on a glass slide. After 9 min, the slides were tilted at 15-45, and the resulting DNA spreads were air dried, fixed in 3:1

methanol/acetic acid, and refrigerated overnight. The DNA fibers were denatured with 2.5 mol HCl for 1 hr, washed with PBS, and blocked with 2 % (w/v) BSA in PBST (PBS and Tween 20) for 40 min. The newly replicated CldU and IdU tracks were labeled (for 2.5 hr in the dark, at RT) with anti-BrdU antibodies recognizing CldU (rat; Abcam) and IdU mouse (BD), respectively. After washing for 533 min in 0.2 % (v/v) PBS-T, the following secondary antibodies were used (1 hr incubation, in the dark, at RT): anti-mouse Alexa Fluor 488 (Molecular Probes) and anti-rat Cy3 (Jackson ImmunoResearch Laboratories, Inc.). After washing for 533 min in PBS-T (0.2 % (v/v)), the slides were air dried completely, mounted with 20 μl per slide Antifade gold (Invitrogen), and sealed to a coverslip by transparent nail polish. Microscopy was performed with a fluorescence microscope (IX81; Olympus; objective lenses: LC Plan Fluor 603, 1.42 NA oil) and acquired with a charge-coupled device camera (Orca AG; Hamamatsu Photonics). The images were processed with CellR software (version 2.6; Olympus). On average 120 fibers were quantified per condition; experiment was repeated twice.

Replication fork protection assay KB2P cells were seeded 24 hr prior the assay to achieve ~75 % confluency. On the next day, cells were pulse-labeled with CldU (25 μmol) for 20 min, washed with warm medium and pulse-labeled with IdU (250 μmol) for another 20 min. Next, cells were incubated for 3 hr with 0.9 μmol MMS to induce replication stress. After MMS incubation, cells were trypsinized, washed and lysed on microscopy slides in lysis buffer (0.5 % (w/v) sodium dodecyl sulfate (SDS), 200 mmol Tris 7.4 pH, 50 mmol EDTA). DNA fibers were spread by tilting the slide, air-dried and fixed in methanol/acetic acid (3:1) for 10 min. Fixed DNA spreads were treated with 2.5 mol HCl for 75 min. Immunofluorescent staining was performed as described in the previous section (RF progression assay). Images were acquired on a Leica DM-6000RXA fluorescence microscope, with Leica Application Suite software. CldU and IdU track lengths were measured using ImageJ software. At least 100 IdU and CldU ratios per condition were analyzed.

Neutral comet assay Asynchronously growing U2OS cells were first incubated with 0.5 μmol olaparib for 1 hr and further treated with 0.5 μmol olaparib alone, or in combination with 1 μmol PDDX-001, for another 60 min. Next, DNA damage was induced by 30 min incubation with 25 nmol CPT in the presence of PARPi and/or PARGi. Cells were then collected by trypsinization and resuspended in PBS at the concentration of 106 cells per ml. 20 μl of cell suspension was then loaded onto 600 μl of 0.8 % (w/v) Low Melting Point (LMP) agarose (Lonza) in PBS, previously equilibrated to 37 °C (for 60 min). Next, 60 μl of cells resuspended in LMP was spread on the comet slide (CometAssay®Kit, Trevigen). Slides were incubated at 4 °C for 15 min to allow solidification of the cells-LMP mixture and further incubated in a lysis buffer (CometAssayO®Lysis Solution, Trevigen) overnight at 4 °C. On the

next day, slides were first incubated in electrophoresis buffer (300 mmol sodium acetate, 100 mmol Tris, 8.3 pH) for 1 hr and then electrophoresis was performed using the comet chamber at 21 Volt for 30 min, at 300 mA and 4 °C. Next, slides were rinsed twice in water, placed in 70 % ethanol at 4 °C for 20 min and incubated at 37 °C until dry. Slides were than stained with SYBR®Gold (Thermo Fisher Scientific) diluted at 1:30,000 in Tris-EDTA (10 mmol Tris-HCl 7.5 pH, 1 mmol EDTA) for 30 min in dark. Images were recorded on a Leica DM6 B upright digital research microscope at 10x magnification. The images were analyzed using the Open Comet plugin (http://www.cometbio.org/) for Fiji. At least 95 cells were analyzed per sample and plotted using GraphPad PRISM 7.0c. The experiment was repeated twice.

Fast micromethod DNA single-strand break assay The assay was performed as described before[40]. Briefly, KB2P1.21 cells were seeded on Corning 96-well special optics plates (#CLS3720, Sigma) 24 hr prior the assay (10,000 cells/well). On the next day, cells were first treated with olaparib and 0.01% MMS for 30 min to induce base damage. After that incubation plates were either processed (time point 0) or further incubated with olaparib for 3 hr (time point 3 hr). Following incubation with drugs, media was removed and cells were incubated for 1 hr in dark with 50 ml of 1 % (v/v) solution of PicoGreen (Thermofisher) in PBS. This incubation was performed at 4 °C to avoid additional DNA repair. After 1 hr 250 μl of NaOH solution, adjusted to a final pH of 12.45 with EDTA, was added to cells and the measurement of the fluorescence signal (485 nm/538 nm) was immediately started using Tecan Infinite 200 PRO (Tecan) plate reader. Measurements were taken every 60 s for 25 min. The data were analyzed as described before[40]. BCA protein measurements were taken to assure equal amount of cells per condition. The experiment was performed in triplicate and repeated twice.

Laser Micro-Irradiation Assays

PARP1-GFP: Multiphoton Laser Mico-Irradiation U2OS cells were transiently transfected (using Lipofectamine 2000, Invitrogen; according to the manufacturer's protocol) with pEGFP-c3-PARP1 (kind gift from Valerie Schreiber) vector. Cells grown on 18 mm coverslips were placed in a Chamlide CMB magnetic chamber and the growth medium was replaced by CO_2-independent Leibovitz's L15 medium supplemented with 10 % (v/v) FCS and penicillin-streptomycin. Cells were treated with DMSO (control), 0.5 μmol olaparib, 1 μmol PDDX-001 or olaparib/PDDX-001 combination for 1 hr prior to micro-irradiation. Laser micro-irradiation was carried out on a Leica SP5 confocal microscope equipped with an environmental chamber set to 37 °C. DSB-containing tracks (1.5 μm width) were generated with a Mira modelocked titanium-sapphire (Ti:Sapphire) laser (l = 800 nm, pulse length =

200 fs, repetition rate = 76 MHz, output power = 80 mW) using a UV-transmitting 633 1.4 NA oil immersion objective (HCX PL APO; Leica). Confocal images were recorded before and after laser irradiation at 5 s or 10 s time intervals over a period of 2-3 min. Images recorded after multi-photon micro-irradiation of living cells were analyzed using ImageJ software. The average pixel intensity of laser tracks was measured within the locally irradiated area function (I_{damage}), in the nucleoplasm outside the locally irradiated area ($I_{\text{nucleoplasm}}$) and in a region not containing cells in the same field of view ($I_{\text{background}}$). The relative level of accumulation expressed relative to the protein level in the nucleoplasm was calculated as follows: $(I_{\text{damage}} - I_{\text{background}}) - (I_{\text{nucleoplasm}} - I_{\text{background}})$.

XRCC1-GFP: UV-A Laser Micro-Irradiation The laser micro-irradiation assay was performed as described before[73]. Briefly, U2OS cells were transiently transfected (using Lipofectamine 2000, Invitrogen; according to the manufacturer's protocol) with pEGFP-C1-XRCC1 (gift from Simon Bekker-Jensen). Cells were grown on 18 mm coverslips and sensitized with 10 μmol 50-bromo-2-deoxyuridine (BrdU) for 24 hr. On the next day, the growth medium was replaced with CO_2-independent Leibovitz's L15 medium supplemented with 10 % FCS and penicillin-streptomycin and cells were kept at 37 °C. Cells were treated with DMSO (control), 0.5 umol olaparib, 1 μmol PDDX-001 or olaparib/PDDX-001 combination for 1 hr prior to micro-irradiation. For micro-irradiation, the cells were placed in a Chamlide TC-A live-cell imaging chamber that was mounted on the stage of a Leica DM IRBE widefield microscope stand (Leica) integrated with a pulsed nitrogen laser (Micropoint Ablation Laser System; Andor). The pulsed nitrogen laser (16 Hz, 364 nm) was directly coupled to the epifluorescence path of the microscope and focused through a Leica 403 HCX PLAN APO 1.25-0.75 oil-immersion objective. The laser output power was set to 60 to generate strictly localized subnuclear DNA damage, resulting in XRCC1, but not in XRCC4 accumulation[73]. Following micro-irradiation, cells were incubated for the indicated time points at 37 °C in Leibovitz's L15 and subsequently fixed with 4 % formaldehyde before immunostaining. Typically, an average of five cells was micro-irradiated (2 iterations per pixel) within 1 min using Andor IQ software (Andor). For each condition, 20-25 cells were micro-irradiated, and experiments were repeated three times (60-75 cells in total). Following DNA damage, cells were further incubated for 5, 10, 15 or 60 min. Next, cells were fixed with 2 % formaldehyde in PBS for 20 min. Cells were post-extracted with 0.5 % Triton-X100 (Sigma) in PBS, and blocked with 20 mmol glycine and 0.5 % BSA in PBS for 15 min and used for antibody incubations. Samples were incubated with primary antibodies overnight at 4 °C and with secondary antibodies supplemented with 0.1 mg ml^{-1} DAPI for 1 hr at room temperature. Samples were subsequently mounted in Polymount (Polysciences). Antibodies used in this study are: primary rabbit polyclonal anti-MDC1 (#ab11171-50, Abcam), diluted 1:1000 and secondary

goat anti-rabbit AlexaFluor-555-conjugated, diluted 1:1500 (#A-21429, Thermo Fisher). The MDC1 (AF-555), XRCC1-GFP (GFP) and CHD2-GFP (GFP) signal was detected using Zeiss AxioImager D2 widefield fluorescence microscope equipped with 403, 633 and 1003 PLAN APO (1.4 NA) oil-immersion objectives (Zeiss) and an HXP 120 metal-halide lamp used for excitation. Images were recorded using the ZEN 2012 software. Tracks were evaluated in ImageJ, by calculating the ratio of track to background (nuclear) intensities for each channel.

PARPi toxicity analysis in a panel of 1,001 cancer cell lines

The pharmacogenomics dataset of 1,001 human cancer cell lines, published recently[41], was used to assess the corelation between PARG or PARP1 expression and IC_{50} values of PARPi. For this purpose, expression data for DDR-related genes (see Table S7.2) and drug response data to olaparib, veliparib, rucaparib and talazoparib was extracted, resulting in a smaller dataset for 935 out of 1,001 cell lines. For statistical analysis Pearson correlation was estimated for each gene and the correlation p values were computed using the relation between the estimated coefficient and the student-t distribution. Negative correlation means that a lower IC_{50} associates with higher expression (= more sensitive).

7.6.4 Quantification and statistical analysis

Statistical parameters including sample size, precision measures and statistical significance are reported in the figures, corresponding figure legends and Method Details sections.

Genetic screens See Figure 7.1, Figure 7.2K and Table S7.1. Genetic screens were performed in triplicate and statistical analysis was carried out using the MAGeCK software.

***In vivo* studies** See Figure 7.2.

Survival analysis The effect of PARPi treatment in mice carrying KB2P tumors was measured by survival analysis of control ($n = 21$) vs AZD2461-treated group ($n = 34$). Data are presented as Kaplan-Meier curves and the p value was computed using Log-Rank (Mantel Cox) statistics (Figure 7.2C).

Statistical analysis of deep-sequencing data See Figure 7.2D, Figure 7.2G, and Figure S7.1. Detailed description of the bioinformatics analysis is reported in the Method Details section.

Immunohistochemistry analysis of PARG expression Semi-quantitative comparison of the PARG staining of resistant ($n = 34$) versus naive ($n = 21$) KB2P tumors was carried out by a trained pathologist who was blinded regarding the sample identity. Group comparison was performed using Mann-Whitney U test. Representative images are shown (Figure 7.2H).

qRT-PCR analysis Gene expression measurements were performed in triplicate, normalized to expression of house keeping genes, and presented as mean $\pm$ SD of replicates. Statistical significance was estimated with the two-tailed unpaired t-test. See Figure 7.3A, Figure 7.6A-B, Figure S7.2A, Figure S7.2E, and Figure S7.3B.

PARG activity assays and PAR ELISA assay Experiments were performed in triplicate, repeated three times and presented as mean $\pm$ SD of repeats. Statistical significance was estimated with the two-tailed unpaired t-test. See Figure 7.2I, Figure 7.3B, and Figure S7.2B for the PARG activity assays and Figure 7.4A for the PAR ELISA assay.

PAR immunofluorescence assay Intensities of PAR signal were measured per nuclei, for four different imaging areas per condition, each containing on average 200 cells; the experiment was repeated three times. Results were presented as a mean for each area (12 areas in total) $\pm$ SD. Statistical analysis was performed using the two-tailed unpaired t-test. See Figure S7.2D.

Long-term clonogenic assays See Figures 7.3C, 7.3E, 7.4F, 7.6F-I, S7.3A, S7.3C, S7.3I, S7.3J, S7.5D, S7.6A, S7.6C, S7.6G, and S7.6H. All experiments were repeated three times, unless otherwise stated, and data are presented as mean $\pm$ SD of replicates. For statistical analysis the two-tailed unpaired t-test (Figures 7.3C, 7.4F, S7.3A, S7.3C, S7.3H, S7.5D, and S7.6A) or ANOVA (Figures 7.3E, S7.6G-J, S7.3G, S7.6B, S7.5F, and S7.6G) test was used.

Analysis of DNA damage-induced foci See Figures S7.5G, S7.4B, and S7.4D. For the analysis of γH2A foci (Figure 7.5G), foci were counted per nuclei, in four different imaging areas per condition, each containing on average 200 cells. Results were presented as a mean $\pm$ SD of the three replicates. Statistical analysis was performed using the two-tailed unpaired t-test. For the analysis of RAD51/53BP1 irradiation-induced foci (Figures S7.4B and S7.4D), foci were counted per nuclei and data are presented as mean $\pm$ SD of replicates (triplicate for cultured cells and five replicates for GEMM samples) and group comparison was performed using the two-tailed unpaired t-test. On average 100 cells were analyzed per replicate.

Fast micromethod SSB assay See Figure 7.5F. Assay was performed in triplicate and repeated twice, data are shown as mean ± SD of the two repeats. Statistical significance was assessed using two-tailed unpaired t-test.

DNA fiber assays See Figures 7.5A, S7.5A, and S7.5I. For the fork protection assay (Figure S7.4A), at least 100 fibers were measured per condition and statistical significance was assessed with the Mann-Whitney U test. For fork progression analysis (Figures 7.4C and S7.5I), on average 120 fibers were quantified and group comparison was performed with the two-tailed unpaired t-test. Experiments were repeated twice.

Neutral comet assay On average 100 comets (cells) were analyzed per condition and each data point represents tail moment (Figure 7.5B) or olive moment (Figure S7.5J) of a single comet, together with a mean ± SD of all cells per condition. Statistical significance was assessed using Mann-Whitney U test. Experiments were repeated twice.

Micro-irradiation assays See Figures 7.4E, 7.5D-E, and S7.5F-G. In each experiment on average 15-20 cells were micro-irradiated and analyzed per condition. Experiments were repeated three times and data are presented as mean ± SEM of independent experiments. Statistical analysis was performed using two-tailed unpaired t-test.

Immunoblotting See Figures 7.2J, 47.4B-C, and S7.5A-B. Immunoblotting experiments were repeated three times. Representative images are shown.

PARPi Toxicity Analysis in a Panel of 1,001 Cancer Cell Lines See Figures 7.6C and S7.6D. Correlation between gene expression and IC_{50} values for PARPi was assessed using Pearson correlation, which was estimated for each gene and the correlation p values were computed using the relation between the estimated coefficient and the student-t distribution.

7.6.5 Data and software availability

The deep sequencing data generated in this study is available in the European Nucleotide Archive (ENA) under accession number PRJEB20535. Raw data from this manuscript: https://doi.org/10.17632/r9cm2kh8mt.1.

7.7 Supplementary Material

7.7.1 Supplementary Figures

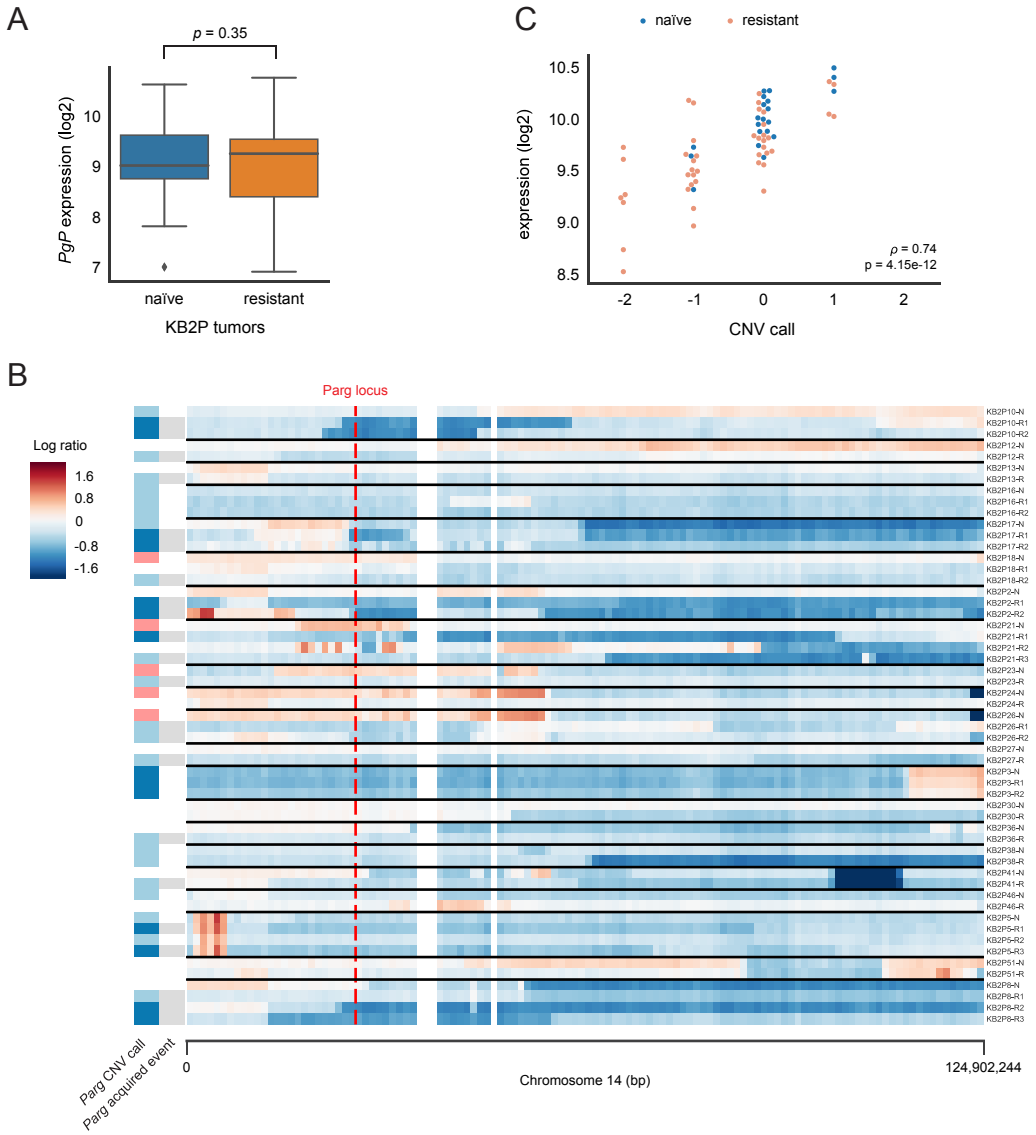

Fig. S7.1. **Multi-omics analysis of PARPi-resistant mouse mammary tumors. Related to Figure 7.2. (A)** Expression (RNA-seq) of Pgp drug efflux transporter in KB2P PARPi-naive and resistant tumors; p value: two-tailed t-test. The box extends from the lower to upper quartile values of the data, with a line at the median; whiskers (whis) are a function of the inner quartile range, they extend to the most extreme data point within (whis $*$ $(75\% - 25\%)$) data range. **(B)** Copy number $\log_2$ ratios of chromosome 14 shown for all KB2P tumors; the *Parg* locus is indicated by the red dashed line. KB2Px-R/Ny: x - original donor ID number, y - ID of individual resistant tumors derived from the same donor tumor, R - resistant, N - naive. **(C)** Correlation between *Parg* expression and copy number estimation for a panel of KB1P tumors. Spearman correlation coefficient (ρ) and p value (DIDS algorithm) are indicated.

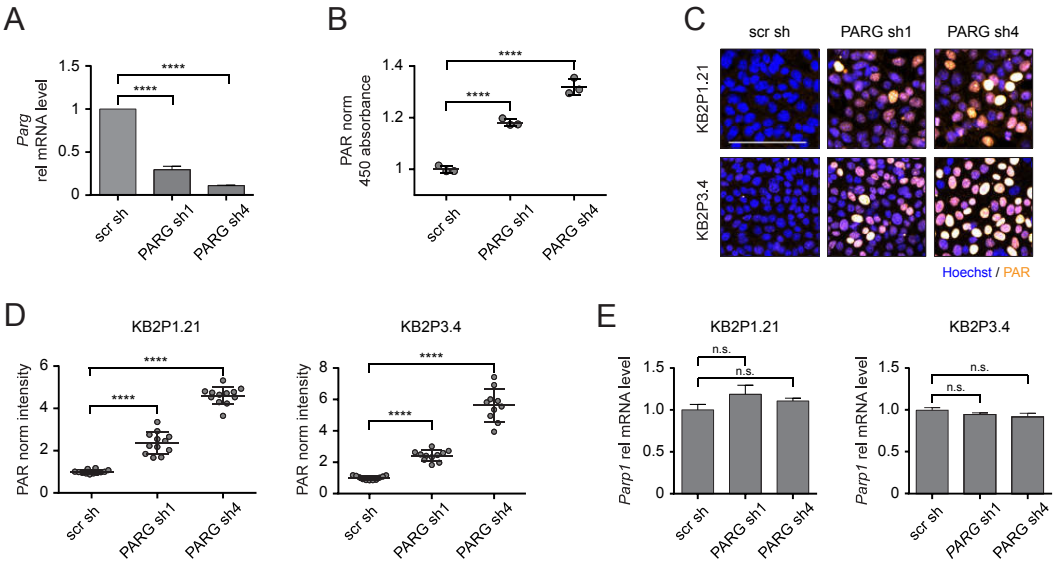

Fig. S7.2. Suppression of PARG in KB2P cells. Related to Figure 7.3. **(A)** RT-qPCR analysis of Parg expression in KB2P3.4 cells expressing indicated shRNAs; $^{****}p < 0.001$ (two-tailed t-test), data shown as mean $\pm$ SD of triplicate. **(B)** ELISA-based PARG activity assay in the cell lines indicated; data represent mean $\pm$ SD of triplicate, $^{****}p < 0.001$ (two-tailed t-test). **(C-D)**Immunofluorescence-based PAR detection in the indicated cell lines upon MMS (0.01 %) treatment. Representative microscopic images (C) and quantification of the assay (D) are shown; $^{****}p < 0.001$ (two-tailed t-test), data are presented as mean $\pm$ SD of single areas imaged (experiment repeated three times, four areas/experiment, average 300 cells/area); scale bar, 100 μm. **(E)** RT-qPCR analysis of *Parp1* gene expression in KB2P PARG kd cells; n.s. - not significant (two tailed t-test), data are shown as mean $\pm$ SD of triplicate experiments.

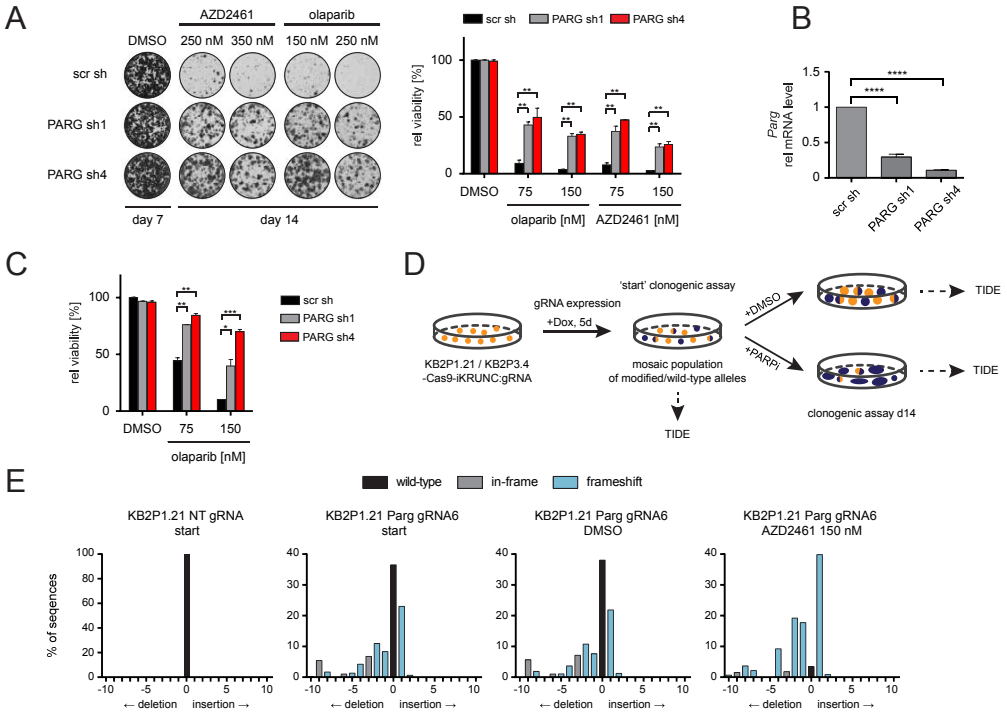

Fig. S7.3. Downregulation of PARG drives PARPi resistance in KB2P cell lines. Related to Figure 7.3. **(A)** Long-term clonogenic assay using KB2P3.4-scr sh (scramble shRNA, control), -PARG sh1 and -PARG sh4 cells and the PARPi AZD2461 or olaparib. Representative images of stained wells (left) and quantification of the assay (right; mean ± SD of three repeats) are shown; $^{**}p < 0.01$ (two-tailed t-test). **(B)** qRT-PCR analysis of *Parg* expression in KB1P-G3 cells expressing the hairpins indicated; $^{****}p < 0.001$ (two-tailed t-test), data shown as mean ± SD of triplicate. **(C)** Clonogenic assay in KB1P-G3 cells expressing the hairpins indicated and treated with olaparib; $^{*}p < 0.05$, $^{**}p < 0.01$, $^{***}p < 0.001$ (two-tailed t-test); data represents mean ± SD of two repeats. **(D)** Outline of the long-term clonogenic assays in KB2P cells expressing control (NT) or gRNAs targeting *Parg*. **(E)** Example of the TIDE analysis: spectrum of alleles identified by the algorithm in the samples indicated.

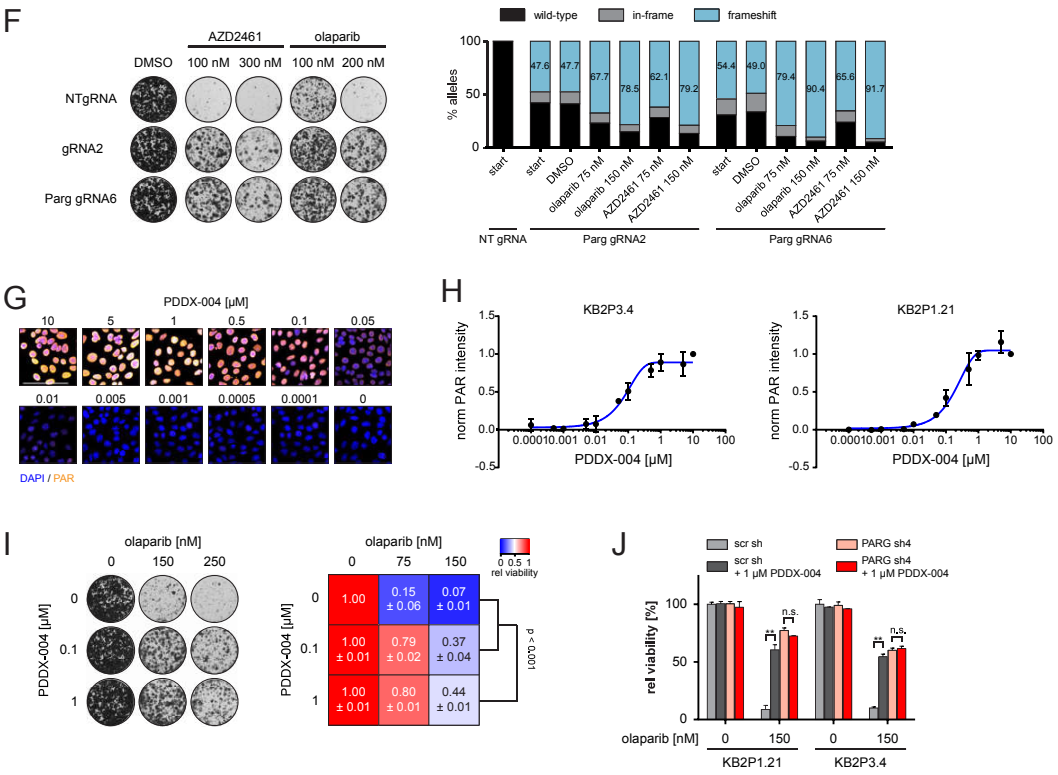

Fig. S7.3. **Continued. (F)** Long-term clonogenic assay using KB2P3.4 cells expressing the indicated gRNAs. Representative images (left) and TIDE quantification of allele composition (right) are shown. **(G-H)** Chemical inhibition of PARG using PDDX-004 in the cell lines indicated. Representative images of PAR immunofluorescent staining (G) and quantification (H) are shown; data represent mean ± SD of three repeats; scale bar, 100 μm. **(I)** Long-term clonogenic assay using KB2P3.4 cells treated with the PARPi olaparib and PARGi PDDX-004 alone or in combination. Representative images of stained cells (left) and quantification of the assay (right) are shown. Data on the graph represent experiments repeated three times (mean ± SD); p value (ANOVA) is indicated. **(J)** Clonogenic assay in KB2P cells expressing the shRNAs indicated, and treated with olaparib; $^{**}p < 0.01$, n.s. - not significant (two-tailed t-test); data shown as mean ± SD of triplicate.

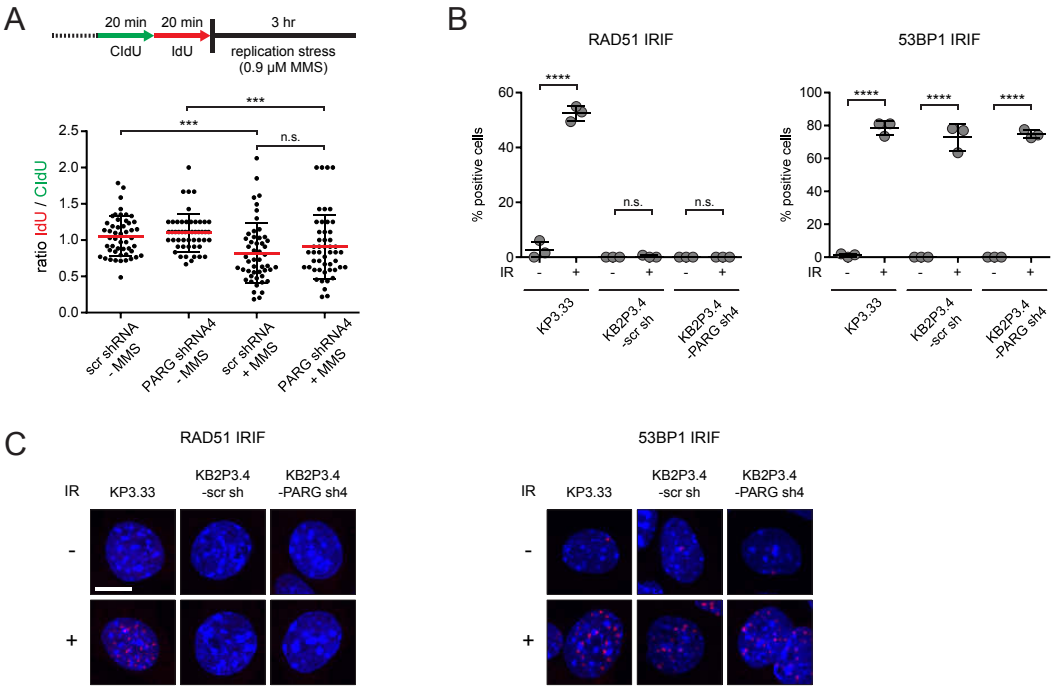

Fig. S7.4. **PARG loss causes PARPi resistance independently of HR and RF protection. Related to Figure 7.4. (A)** DNA fiber assay using KB2P3.4 cells treated with MMS (0.9 μmol); $^{***}p < 0.001$, n.s. - not significant (Mann-Whitney U test). Error bars represent SD and red lines represent mean values. **(B-C)** RAD51/53BP1 IRIF formation assay in the given cell lines; KP3.33 ($p53^{-/-}$) cells were used as HR-proficient control in this assay; 53BP1 served as DNA damage marker. Quantification (B) and representative images (C) are shown. A cell was considered positive when: RAD51 $\geq$ 5 foci/nuclei, 53BP1 $\geq$ 10 foci/nuclei. Data represent mean $\pm$ SD; $^{****}p < 0.0001$, n.s. - not significant (two-tailed t-test); scale bar, 10 μm.

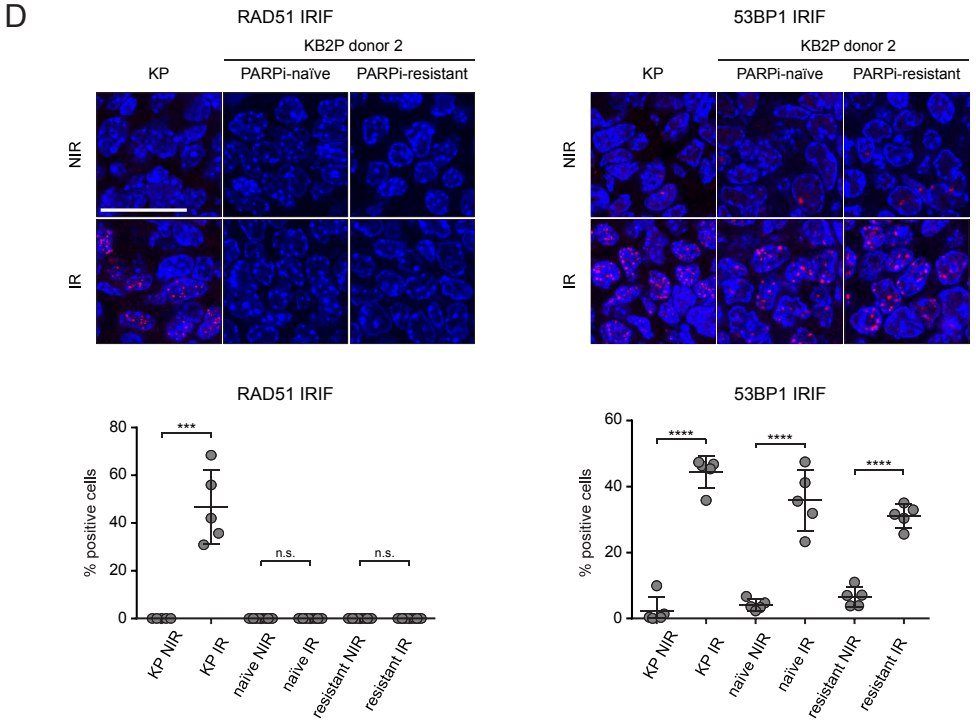

Fig. S7.4. **Continued. (D)** Example of RAD51 foci formation analysis in a KB2P2 tumor pair, representative for all PARPi-resistant tumors for which alterations in the *Parg* gene were identified by DeepSeq analysis. Matched naive samples, as well as KP ($p53^{-/-}$) tumor (positive control) were taken along for the analysis. Microscopy images (upper panels) and foci quantification (lower panels) are shown. For quantification, a fraction of positive cells ($\geq$ 5 foci/nuclei for RAD51 and $\geq$ 10 foci/nuclei for 53BP1) was calculated for five different areas of each tumor (shown as single data point on the graph, error bars represent SD). $^{***}p < 0.0001$, $^{****}p < 0.0001$, n.s. - not significant (two-tailed t-test). 53BP1 was used as a marker of DNA damage. Scale bar, 25 μm.

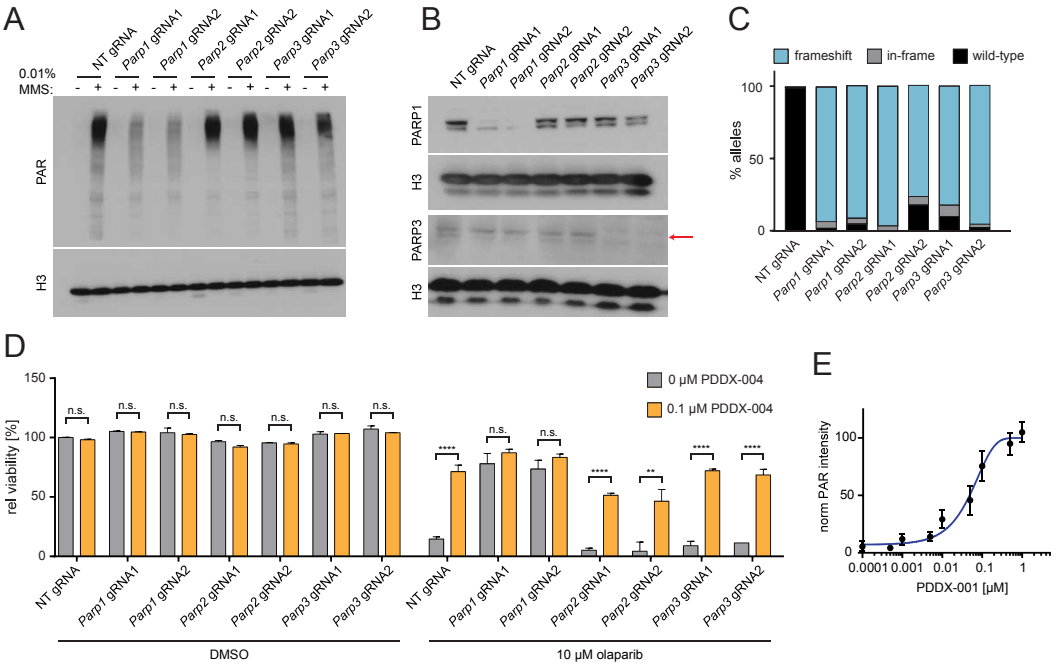

Fig. S7.5. **PARG depletion partially restores downstream signaling of PARP1. Related to Figures 7.4 and 7.5. (A-B)** Immunoblot analysis of PAR (A), PARP1 and PARP3 (B) cellular levels in KP3.33 expressing the gRNAs indicated. Red arrow (B) indicates band specific for PARP3. Histone 3 (H3) was used as a loading control. Data representative of experiments repeated twice. **(C)** TIDE analysis of allele modification rates in KP3.33 cells expressing the gRNAs indicated; data representative for experiment repeated twice. **(D)** Clonogenic assay with KP3.33 cells expressing the gRNAs indicated, treated with olaparib; $^{**}p < 0.01$, $^{****}p < 0.0001$, n.s. - not significant; data shown as mean ± SD of two repeats. **(E)** PARG inhibition in U2OS cells by PDDX-001; data presented as mean ± SD of two repeats.

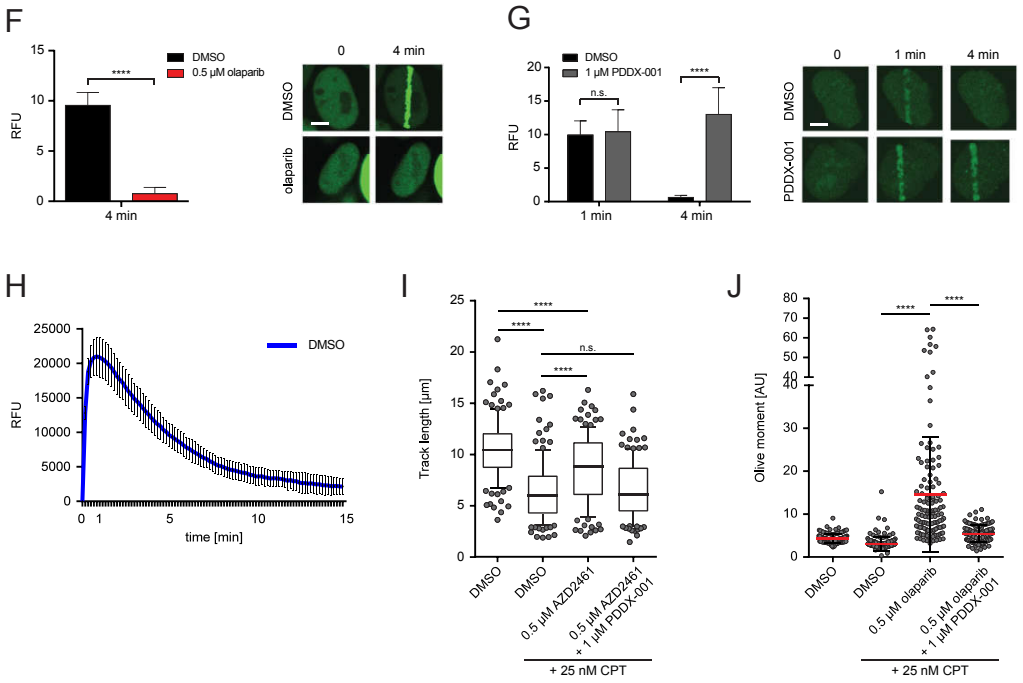

Fig. S7.5. **Continued. (F)** GFP-XRCC1 recruitment analysis in DMSO (control) or olaparib-treated GFP-XRCC1 U2OS cells; representative images (right) and quantification (left) are shown. XRCC1 recruitment was used as a readout for PARP1 inhibition. **(G)** GFP-CHD2 binding to the site of DNA damage in GFP-CHD2 U2OS cells treated with DMSO (control) or PDDX-001; representative images (right) and quantification (left panel) are shown. CHD2 association to chromatin was used as a positive control for PARG inhibition. **(H)** Time-course recruitment analysis of GFP-PARP1 to laser tracks in control cells (DMSO). For experiments shown in (F-H) data are represented as mean $\pm$ SEM of two independent repeats; $^{****}p < 0.0001$ (t-test); in all images scale bar, 10 μm. **(I)** Fork progression assay in U2OS cells exposed to the treatments indicated. Box extends from 25$^{\text{th}}$ to 75$^{\text{th}}$ percentile, with a middle line representing the median and whiskers drawn down to the 10$^{\text{th}}$ percentile and up to the 90$^{\text{th}}$. **(J)** Neutral comet assay in U2OS cells treated as indicated. Data shown as mean $\pm$ SD of a replicate. Experiments shown in (I-J) were repeated twice; $^{****}p < 0.001$, n.s. - not significant, Mann-Whitney U test.

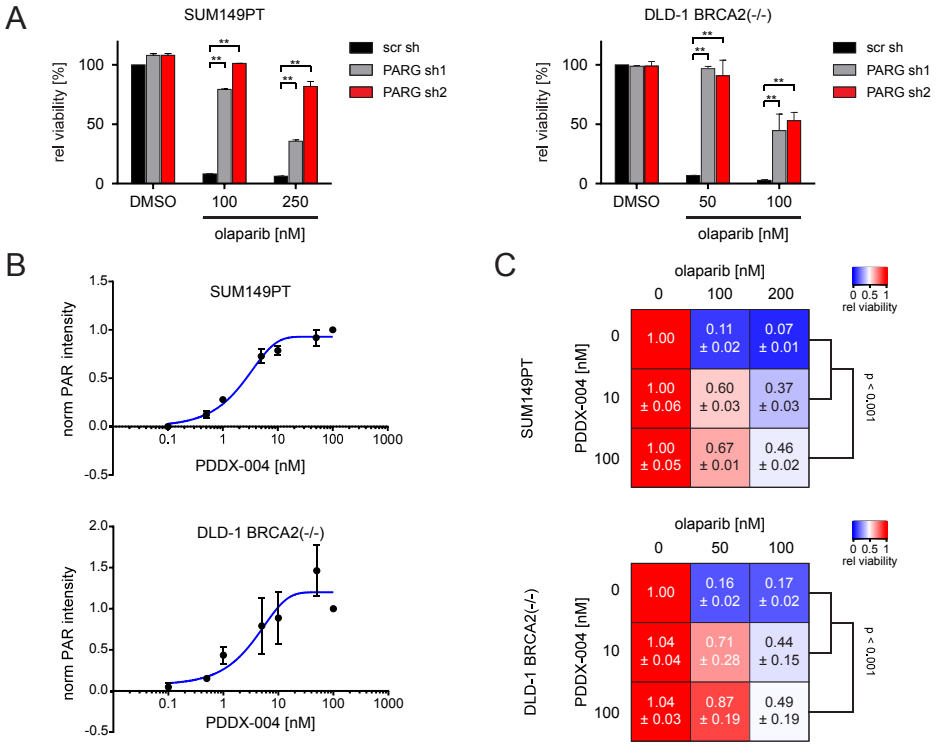

Fig. S7.6. PARPi response of PARG-depleted human cancer cells. Related to Figure 7.6. **(A)** Quantification of long-term clonogenic assays shown in Figure 7.5A. Graph represents mean ± SD values of triplicates; $^{**}p < 0.01$ (two-tailed t-test). **(B)** Chemical inhibition of PARG with PDDX-004 in indicated cells. Data represent mean ± SD of three repeats. **(C)** Quantification of a long-term clonogenic assay in SUM149PT (upper panel) and DLD-1 BRCA2(-/-) (lower panel) cells treated with the PARPi olaparib and the PARGi PDDX-004 alone or in combination. Data presented as mean ± SD values of three repeats.

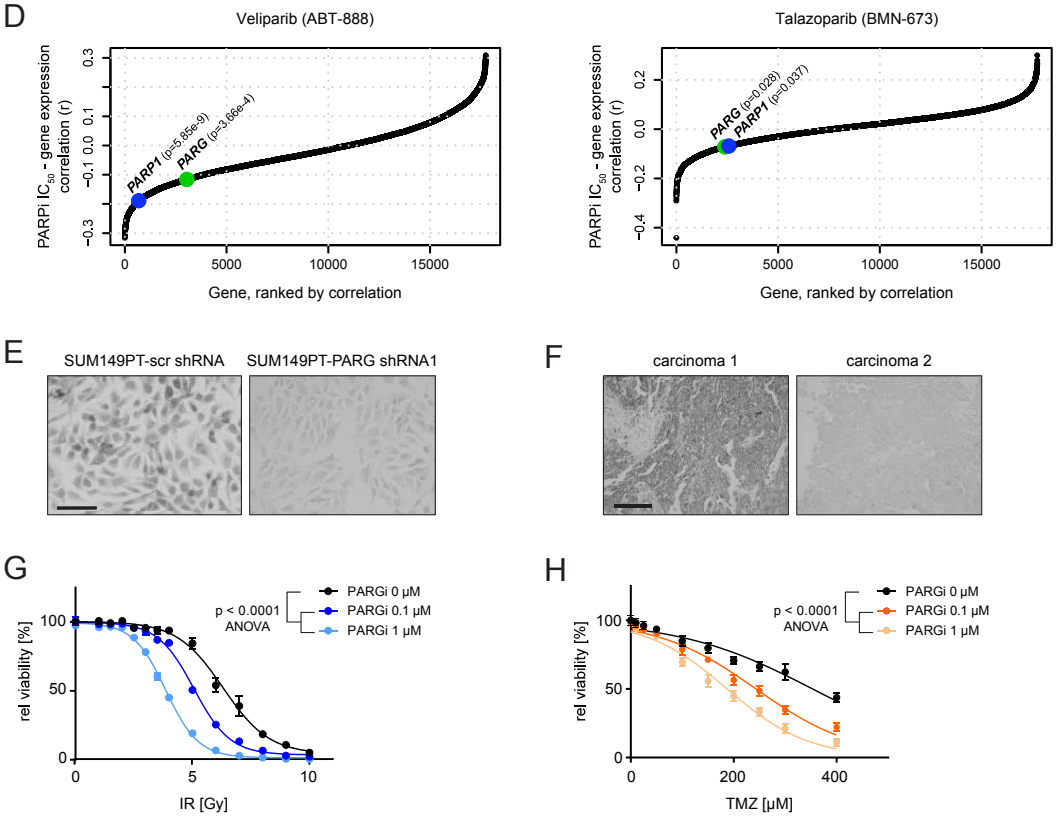

Fig. S7.6. **Continued. (D)** Correlation analysis between IC_{50} values of PARPi (veliparib and talazoparib) and expression of DDR genes in a panel of 935 human cancer cell lines; *PARP1* and *PARG* are highlighted; Pearson correlation was computed and p values were determined using the relation between estimated coefficient and the student-t distribution. **(E)** Validation of PARG antibody used in IHC analyses; representative images of SUM149PT cells expressing indicated shRNAs are shown; scale bar, 100 μm. **(F)** Example of PARG IHC staining in two ovarian serous carcinomas; scale bar, 100 μm. **(G-H)** Response of KB2P1.21 cells to ionizing radiation (IR) and temozolomide (TMZ), treated with PARGi PDDX-004. Data is presented as mean $\pm$ SD.

7.7.2 Supplementary Tables (available online)

Tab. S7.1. Genetic screens identify *Parg* as a PARPi-resistance factor. Related to Figures 7.1 and 7.2.

Tab. S7.2. DDR-related genes. Related to Figures 7.2 and 7.6.

Tab. S7.3. Overview of candidate genes identified in multi-omics analysis of matched KB2P PARPi-naive and -resistant tumors. Related to Figure 7.2.

Tab. S7.4. Custom-made shRNA library targeting candidate genes (identified by multi-omics analysis of KB2P tumors) and additional 32 non-essential genes (controls). Related to Figure 7.2.

Tab. S7.5. TIDE analysis of clonogenic assays using KB2P cells expressing gRNAs targeting *Parg*. Related to Figure 7.3.

Tab. S7.6. Oligonucleotides used in this study. Related to STAR methods.

7.8 References

[1] Felix Dietlein, Lisa Thelen, and H Christian Reinhardt. “Cancer-specific defects in DNA repair pathways as targets for personalized therapeutic approaches”. In: *Trends in Genetics* 30.8 (2014), pp. 326–339 (cit. on p. 230).

[2] Helen E Bryant, Niklas Schultz, Huw D Thomas, et al. “Specific killing of BRCA2-deficient tumours with inhibitors of poly (ADP-ribose) polymerase”. In: *Nature* 434.7035 (2005), pp. 913–917 (cit. on pp. 230, 231).

[3] Hannah Farmer, Nuala McCabe, Christopher J Lord, et al. “Targeting the DNA repair defect in BRCA mutant cells as a therapeutic strategy”. In: *Nature* 434.7035 (2005), pp. 917–921 (cit. on pp. 230, 231).

[4] Bryan A Gibson and W Lee Kraus. “New insights into the molecular and cellular functions of poly (ADP-ribose) and PARPs”. In: *Nature Reviews Molecular Cell Biology* 13.7 (2012), pp. 411–424 (cit. on p. 230).

[5] John M Pascal and Tom Ellenberger. “The rise and fall of poly (ADP-ribose): an enzymatic perspective”. In: *DNA Repair* 32 (2015), pp. 10–16 (cit. on pp. 231, 239).

[6] Guotai Xu, Jos Jonkers, and Sven Rottenberg. “PARP Inhibitor Resistance—What Is Beyond BRCA1 or BRCA2 Restoration?” In: *PARP Inhibitors for Cancer Therapy*. Springer, 2015, pp. 453–471 (cit. on p. 231).

[7] Junko Murai, N Huang Shar-yin, Benu Brata Das, et al. “Trapping of PARP1 and PARP2 by clinical PARP inhibitors”. In: *Cancer Research* 72.21 (2012), pp. 5588–5599 (cit. on pp. 231, 239, 259).

[8] Junko Murai, Shar-Yin N Huang, Amèlie Renaud, et al. “Stereospecific PARP trapping by BMN 673 and comparison with olaparib and rucaparib”. In: *Molecular Cancer Therapeutics* 13.2 (2014), pp. 433–443 (cit. on pp. 231, 246).

[9] Bastiaan Evers, Rinske Drost, Eva Schut, et al. “Selective inhibition of BRCA2-deficient mammary tumor cell growth by AZD2281 and cisplatin”. In: *Clinical Cancer Research* 14.12 (2008), pp. 3916–3925 (cit. on pp. 231, 232, 251).

[10] Sven Rottenberg, Janneke E Jaspers, Ariena Kersbergen, et al. “High sensitivity of BRCA1-deficient mammary tumors to the PARP inhibitor AZD2281 alone and in combination with platinum drugs”. In: *Proceedings of the National Academy of Sciences* 105.44 (2008), pp. 17079–17084 (cit. on p. 231).

[11] M William Audeh, James Carmichael, Richard T Penson, et al. “Oral poly (ADP-ribose) polymerase inhibitor olaparib in patients with BRCA1 or BRCA2 mutations and recurrent ovarian cancer: a proof-of-concept trial”. In: *The Lancet* 376.9737 (2010), pp. 245–251 (cit. on p. 231).

[12] Peter C Fong, David S Boss, Timothy A Yap, et al. “Inhibition of poly (ADP-ribose) polymerase in tumors from BRCA mutation carriers”. In: *New England Journal of Medicine* 361.2 (2009), pp. 123–134 (cit. on p. 231).

[13] Andrew Tutt, Mark Robson, Judy E Garber, et al. “Oral poly (ADP-ribose) polymerase inhibitor olaparib in patients with BRCA1 or BRCA2 mutations and advanced breast cancer: a proof-of-concept trial”. In: *The Lancet* 376.9737 (2010), pp. 235–244 (cit. on p. 231).

[14] Akihiro Ohmoto and Shinichi Yachida. “Current status of poly (ADP-ribose) polymerase inhibitors and future directions”. In: *OncoTargets and Therapy* 10 (2017), p. 5195 (cit. on p. 231).

[15] Stefano Annunziato, Marco Barazas, Sven Rottenberg, and Jos Jonkers. “Genetic dissection of cancer development, therapy response, and resistance in mouse models of breast cancer”. In: *Cold Spring Harbor Symposia on Quantitative Biology*. Vol. 81. Cold Spring Harbor Laboratory Press. 2016, pp. 141–150 (cit. on p. 231).

[16] Stacey L Edwards, Rachel Brough, Christopher J Lord, et al. “Resistance to therapy caused by intragenic deletion in BRCA2”. In: *Nature* 451.7182 (2008), pp. 1111–1115 (cit. on p. 231).

[17] Elizabeth M Swisher, Wataru Sakai, Beth Y Karlan, et al. “Secondary BRCA1 mutations in BRCA1-mutated ovarian carcinomas with platinum resistance”. In: *Cancer Research* 68.8 (2008), pp. 2581–2586 (cit. on p. 231).

[18] Joo Ern Ang, Charlie Gourley, C Bethan Powell, et al. “Efficacy of chemotherapy in BRCA1/2 mutation carrier ovarian cancer in the setting of PARP inhibitor resistance: a multi-institutional study”. In: *Clinical Cancer Research* 19.19 (2013), pp. 5485–5493 (cit. on p. 231).

[19] Stephen J Pettitt, Farah L Rehman, Ilirjana Bajrami, et al. “A genetic screen using the PiggyBac transposon in haploid cells identifies Parp1 as a mediator of olaparib toxicity”. In: *PloS One* 8.4 (2013), e61520 (cit. on pp. 231, 247).

[20] Jos Jonkers, Ralph Meuwissen, Hanneke van der Gulden, et al. “Synergistic tumor suppressor activity of BRCA2 and p53 in a conditional mouse model for breast cancer”. In: *Nature Genetics* 29.4 (2001), pp. 418–425 (cit. on pp. 232, 250, 252).

[21] Alexandra A Duarte, Ewa Gogola, Norman Sachs, et al. “BRCA-deficient mouse mammary tumor organoids to study cancer-drug resistance”. In: *Nature Methods* 15.2 (2018), p. 134 (cit. on pp. 232, 233, 251, 256).

[22] Guotai Xu, J Ross Chapman, Inger Brandsma, et al. “REV7 counteracts DNA double-strand break resection and affects PARP inhibition”. In: *Nature* 521.7553 (2015), pp. 541–544 (cit. on pp. 232, 247, 255, 257, 260, 261).

[23] Wei Li, Han Xu, Tengfei Xiao, et al. “MAGeCK enables robust identification of essential genes from genome-scale CRISPR/Cas9 knockout screens”. In: *Genome Biology* 15.12 (2014), p. 554 (cit. on pp. 232, 257).

[24] Janneke E Jaspers, Ariena Kersbergen, Ute Boon, et al. “Loss of 53BP1 causes PARP inhibitor resistance in Brca1-mutated mouse mammary tumors”. In: *Cancer Discovery* 3.1 (2013), pp. 68–81 (cit. on pp. 233, 236, 250, 251).

[25] Lenka Oplustil O’Connor, Stuart L Rulten, Aaron N Cranston, et al. “The PARP inhibitor AZD2461 provides insights into the role of PARP3 inhibition for both synthetic lethality and tolerability with chemotherapy in preclinical models”. In: *Cancer Research* 76.20 (2016), pp. 6084–6094 (cit. on p. 233).

[26] Arnab Ray Chaudhuri, Elsa Callen, Xia Ding, et al. “Replication fork stability confers chemoresistance in BRCA-deficient cells”. In: *Nature* 535.7612 (2016), pp. 382–387 (cit. on pp. 233, 237).

[27] Jorma J de Ronde, Guillem Rigaill, Sven Rottenberg, Sjoerd Rodenhuis, and Lodewyk FA Wessels. “Identifying subgroup markers in heterogeneous populations”. In: *Nucleic Acids Research* 41.21 (2013), e200–e200 (cit. on pp. 234, 253).

[28] Raivo Kolde, Sven Laur, Priit Adler, and Jaak Vilo. “Robust rank aggregation for gene list integration and meta-analysis”. In: *Bioinformatics* 28.4 (2012), pp. 573–580 (cit. on p. 234).

[29] Eva K Brinkman, Tao Chen, Mario Amendola, and Bas van Steensel. “Easy quantitative assessment of genome editing by sequence trace decomposition”. In: *Nucleic Acids Research* 42.22 (2014), e168–e168 (cit. on pp. 236, 257).

[30] Dominic I James, Kate M Smith, Allan M Jordan, et al. “First-in-class chemical probes against poly (ADP-ribose) glycohydrolase (PARG) inhibit DNA repair with differential pharmacology to Olaparib”. In: *ACS Chemical Biology* 11.11 (2016), pp. 3179–3190 (cit. on pp. 237, 240).

[31] Mi Young Kim, Tong Zhang, and W Lee Kraus. “Poly (ADP-ribosyl) ation by PARP-1:PAR-laying’NAD+ into a nuclear signal”. In: *Genes & Development* 19.17 (2005), pp. 1951–1967 (cit. on p. 239).

[32] Kazuto Sugimura, Shin-ichiro Takebayashi, Hiroshi Taguchi, Shunichi Takeda, and Katsuzumi Okumura. “PARP-1 ensures regulation of replication fork progression by homologous recombination on damaged DNA”. In: *Journal Cell of Biology* 183.7 (2008), pp. 1203–1212 (cit. on p. 241).

[33] Arnab Ray Chaudhuri, Yoshitami Hashimoto, Raquel Herrador, et al. “Topoisomerase I poisoning results in PARP-mediated replication fork reversal”. In: *Nature Structural & Molecular Biology* 19.4 (2012), pp. 417–423 (cit. on p. 241).

[34] Matteo Berti, Arnab Ray Chaudhuri, Saravanabhavan Thangavel, et al. “Human RECQ1 promotes restart of replication forks reversed by DNA topoisomerase I inhibition”. In: *Nature Structural & Molecular Biology* 20.3 (2013), pp. 347–354 (cit. on pp. 241, 247).

[35] Ralph Zellweger, Damian Dalcher, Karun Mutreja, et al. “Rad51-mediated replication fork reversal is a global response to genotoxic treatments in human cells”. In: *Journal of Cell Biology* 208.5 (2015), pp. 563–579 (cit. on pp. 241, 247, 261).

[36] Kai J Neelsen and Massimo Lopes. “Replication fork reversal in eukaryotes: from dead end to dynamic response”. In: *Nature Reviews Molecular Cell Biology* 16.4 (2015), pp. 207–220 (cit. on pp. 241, 247).

[37] Zhanna K Nazarkina, Svetlana N Khodyreva, Stéphanie Marsin, Olga I Lavrik, and J Pablo Radicella. “XRCC1 interactions with base excision repair DNA intermediates”. In: *DNA Repair* 6.2 (2007), pp. 254–264 (cit. on p. 241).

[38] In-Kwon Kim, Roderick A Stegeman, Chris A Brosey, and Tom Ellenberger. “A quantitative assay reveals ligand specificity of the DNA scaffold repair protein XRCC1 and efficient disassembly of complexes of XRCC1 and the poly (ADP-ribose) polymerase 1 by poly (ADP-ribose) glycohydrolase”. In: *Journal of Biological Chemistry* 290.6 (2015), pp. 3775–3783 (cit. on p. 241).

[39] Qingsheng Yan, Rong Xu, Liya Zhu, et al. “BAL1 and its partner E3 ligase, BBAP, link Poly (ADP-ribose) activation, ubiquitylation, and double-strand DNA repair independent of ATM, MDC1, and RNF8”. In: *Molecular and Cellular Biology* 33.4 (2013), pp. 845–857 (cit. on p. 242).

[40] Heinz C Schröder, Renato Batel, Heiko Schwertner, Oleksandra Boreiko, and Werner EG Müller. “Fast micromethod DNA single-strand-break assay”. In: *DNA Repair Protocols*. Springer, 2006, pp. 287–305 (cit. on pp. 242, 263).

[41] Francesco Iorio, Theo A Knijnenburg, Daniel J Vis, et al. “A landscape of pharmacogenomic interactions in cancer”. In: *Cell* 166.3 (2016), pp. 740–754 (cit. on pp. 242, 265).

[42] Teresa Cabezón, Irina Gromova, Pavel Gromov, et al. “Proteomic profiling of triple-negative breast carcinomas in combination with a three-tier orthogonal technology approach identifies Mage-A4 as potential therapeutic target in estrogen receptor negative breast cancer”. In: *Molecular & Cellular Proteomics* 12.2 (2013), pp. 381–394 (cit. on pp. 243, 250).

[43] Irina Gromova, Pavel Gromov, Naoko Honma, et al. “High level PHGDH expression in breast is predominantly associated with keratin 5-positive cell lineage independently of malignancy”. In: *Molecular Oncology* 9.8 (2015), pp. 1636–1654 (cit. on pp. 243, 250).

[44] Pavel Moudry, Kenji Watanabe, Kamila M Wolanin, et al. “TOPBP1 regulates RAD51 phosphorylation and chromatin loading and determines PARP inhibitor sensitivity”. In: *Journal of Cell Biology* 212.3 (2016), pp. 281–288 (cit. on pp. 244, 251).

[45] Jean-Christophe Amé, Elise Fouquerel, Laurent R Gauthier, et al. “Radiation-induced mitotic catastrophe in PARG-deficient cells”. In: *Journal of Cell Science* 122.12 (2009), pp. 1990–2002 (cit. on pp. 245, 248).

[46] Charlene Kan and Junran Zhang. “BRCA1 Mutation: A Predictive Marker for Radiation Therapy?” In: *International Journal of Radiation Oncology * Biology * Physics* 93.2 (2015), pp. 281–293 (cit. on p. 245).

[47] Fabricio G Sousa, Renata Matuo, Daniele G Soares, et al. “PARPs and the DNA damage response”. In: *Carcinogenesis* 33.8 (2012), pp. 1433–1440 (cit. on p. 246).

[48] Silvana De Lorenzo, Anand Patel, Rachel Hurley, and Scott HMD Kaufmann. “The elephant and the blind men: making sense of PARP inhibitors in homologous recombination deficient tumor cells”. In: *Frontiers in Oncology* 3 (2013), p. 228 (cit. on p. 247).

[49] Julie K Horton, Mary Watson, Donna F Stefanick, et al. “XRCC1 and DNA polymerase β in cellular protection against cytotoxic DNA single-strand breaks”. In: *Cell Research* 18.1 (2008), pp. 48–63 (cit. on p. 247).

[50] Nilufer Jasmine Selimah Fauzee, Juan Pan, and Ya-lan Wang. “PARP and PARG inhibitors—new therapeutic targets in cancer treatment”. In: *Pathology & Oncology Research* 16.4 (2010), pp. 469–478 (cit. on p. 247).

[51] Catherine Fathers, Ross M Drayton, Svetlana Solovieva, and Helen E Bryant. “Inhibition of poly (ADP-ribose) glycohydrolase (PARG) specifically kills BRCA2-deficient tumor cells”. In: *Cell Cycle* 11.5 (2012), pp. 990–997 (cit. on p. 247).

[52] Aurélia Noll, Giuditta Illuzzi, Jean-Christophe Amé, Françoise Dantzer, and Valérie Schreiber. “PARG deficiency is neither synthetic lethal with BRCA1 nor PTEN deficiency”. In: *Cancer Cell International* 16.1 (2016), p. 53 (cit. on p. 247).

[53] Polly Gravells, Emma Grant, Kate M Smith, Dominic I James, and Helen E Bryant. “Specific killing of DNA damage-response deficient cells with inhibitors of poly (ADP-ribose) glycohydrolase”. In: *DNA Repair* 52 (2017), pp. 81–91 (cit. on p. 247).

[54] David W Koh, Ann M Lawler, Marc F Poitras, et al. “Failure to degrade poly (ADP-ribose) causes increased sensitivity to cytotoxicity and early embryonic lethality”. In: *Proceedings of the National Academy of Sciences* 101.51 (2004), pp. 17699–17704 (cit. on p. 247).

[55] Christopher J Lord and Alan Ashworth. “PARP inhibitors: Synthetic lethality in the clinic”. In: *Science* 355.6330 (2017), pp. 1152–1158 (cit. on p. 248).

[56] Amy Drean, Christopher J Lord, and Alan Ashworth. “PARP inhibitor combination therapy”. In: *Critical Reviews in Oncology/Hematology* 108 (2016), pp. 73–85 (cit. on p. 248).

[57] Toshiro Sato, Robert G Vries, Hugo J Snippert, et al. “Single Lgr5 stem cells build crypt villus structures in vitro without a mesenchymal niche”. In: *Nature* 459.7244 (2009), pp. 262–265 (cit. on p. 251).

[58] Sven Rottenberg, Anders OH Nygren, Marina Pajic, et al. “Selective induction of chemotherapy resistance of mammary tumors in a conditional mouse model for hereditary breast cancer”. In: *Proceedings of the National Academy of Sciences* 104.29 (2007), pp. 12117–12122 (cit. on p. 252).

[59] Marcel Martin. “Cutadapt removes adapter sequences from high-throughput sequencing reads”. In: *EMBnet. journal* 17.1 (2011), pp. 10–12 (cit. on pp. 253, 254).

[60] Alexander Dobin, Carrie A Davis, Felix Schlesinger, et al. “STAR: ultrafast universal RNA-seq aligner”. In: *Bioinformatics* 29.1 (2013), pp. 15–21 (cit. on p. 253).

[61] S. Andrews. *FastQC: a quality control tool for high throughput sequence data*. 2017. URL: `http://www.bioinformatics.bbsrc.ac.uk/projects/fastqc` (cit. on pp. 253, 254).

[62] Philip Ewels, Måns Magnusson, Sverker Lundin, and Max Käller. “MultiQC: summarize analysis results for multiple tools and samples in a single report”. In: *Bioinformatics* 32.19 (2016), pp. 3047–3048 (cit. on pp. 253, 254).

[63] Yang Liao, Gordon K Smyth, and Wei Shi. “featureCounts: an efficient general purpose program for assigning sequence reads to genomic features”. In: *Bioinformatics* 30.7 (2014), pp. 923–930 (cit. on p. 253).

[64] Michael I Love, Wolfgang Huber, and Simon Anders. “Moderated estimation of fold change and dispersion for RNA-seq data with DESeq2”. In: *Genome Biology* 15.12 (2014), pp. 1–21 (cit. on p. 253).

[65] Heng Li and Richard Durbin. “Fast and accurate short read alignment with Burrows–Wheeler transform”. In: *Bioinformatics* 25.14 (2009), pp. 1754–1760 (cit. on p. 254).

[66] Heng Li, Bob Handsaker, Alec Wysoker, et al. “The sequence alignment/map format and SAMtools”. In: *Bioinformatics* 25.16 (2009), pp. 2078–2079 (cit. on p. 254).

[67] Ilari Scheinin, Daoud Sie, Henrik Bengtsson, et al. “DNA copy number analysis of fresh and formalin-fixed specimens by shallow whole-genome sequencing with identification and exclusion of problematic regions in the genome assembly”. In: *Genome Research* 24.12 (2014), pp. 2022–2032 (cit. on p. 254).

[68] Raivo Kolde and Sven Laur. *RobustRankAggreg: Methods for robust rank aggregation*. R package version 1.1. 2013 (cit. on p. 254).

[69] Jirina Bartkova, Zuzana Horejsi, Karen Koed, et al. “DNA damage response as a candidate anti-cancer barrier in early human tumorigenesis”. In: *Nature* 434.7035 (2005), pp. 864–870 (cit. on p. 255).

[70] Traver Hart, Kevin R Brown, Fabrice Sircoulomb, Robert Rottapel, and Jason Moffat. “Measuring error rates in genomic perturbation screens: gold standards for human functional genomics”. In: *Molecular Systems Biology* 10.7 (2014), p. 733 (cit. on p. 255).

[71] Anirudh Prahallad, Guus JJE Heynen, Giovanni Germano, et al. “PTPN11 is a central node in intrinsic and acquired resistance to targeted cancer drugs”. In: *Cell Reports* 12.12 (2015), pp. 1978–1985 (cit. on p. 256).

[72] Neville E Sanjana, Ophir Shalem, and Feng Zhang. “Improved vectors and genome-wide libraries for CRISPR screening”. In: *Nature Methods* 11.8 (2014), pp. 783–784 (cit. on p. 256).

[73] Martijn S Luijsterburg, Inge de Krijger, Wouter W Wiegant, et al. “PARP1 links CHD2-mediated chromatin expansion and H3. 3 deposition to DNA repair by non-homologous end-joining”. In: *Molecular Cell* 61.4 (2016), pp. 547–562 (cit. on pp. 256, 264).

[74] Antonia Follenzi, Laurie E Ailles, Silvia Bakovic, Massimo Geuna, and Luigi Naldini. “Gene transfer by lentiviral vectors is limited by nuclear translocation and rescued by HIV-1 pol sequences”. In: *Nature Genetics* 25.2 (2000), pp. 217–222 (cit. on p. 256).

[75] Marco Barazas, Stefano Annunziato, Stephen J Pettitt, et al. “The CST complex mediates end protection at double-strand breaks and promotes PARP inhibitor sensitivity in BRCA1-deficient cells”. In: *Cell Reports* 23.7 (2018), pp. 2107–2118 (cit. on p. 258).

[76] Dominic I James, Stephen Durant, Kay Eckersley, et al. “An assay to measure poly (ADP ribose) glycohydrolase (PARG) activity in cells”. In: *F1000 Research* 5 (2016) (cit. on p. 259).